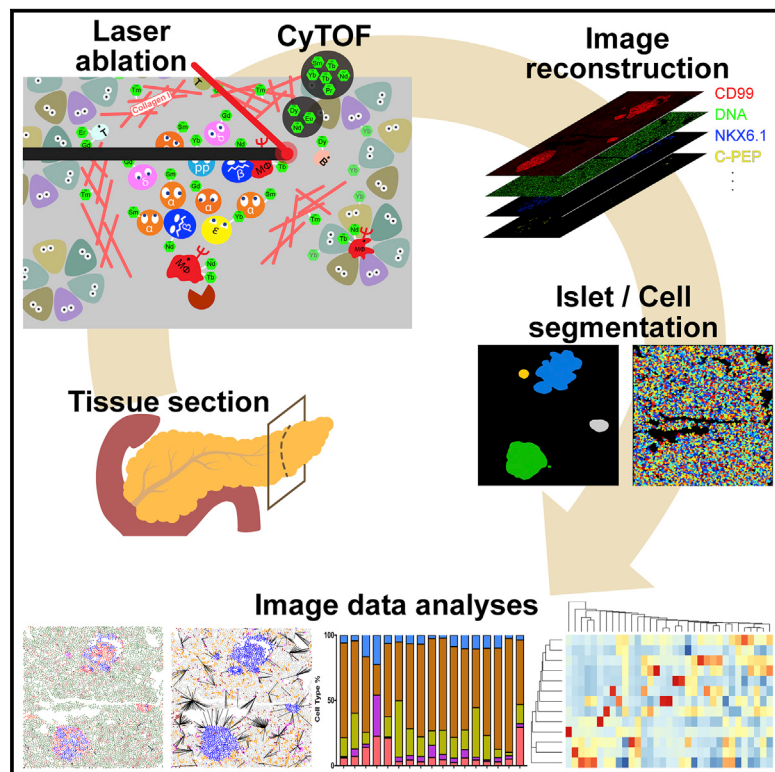


Cell Metabolism

Multiplexed *In Situ* Imaging Mass Cytometry Analysis of the Human Endocrine Pancreas and Immune System in Type 1 Diabetes

Graphical Abstract



Authors

Yue J. Wang, Daniel Traum,
Jonathan Schug, ..., Ali Naji,
Kyong-Mi Chang, Klaus H. Kaestner

Correspondence

kaestner@pennmedicine.upenn.edu

In Brief

Wang et al. use imaging mass cytometry (IMC) to profile the pancreata of type 1 diabetes donors at varying stages of disease progression. They see significant alterations in islet architecture, endocrine cell composition, and immune cell presentation, highlighting the utility of IMC to dissect cellular events underlying disease pathology.

Highlights

- Imaging mass cytometry enables multiplexed histological analyses at 1- μm resolution
- Islets are altered in architecture and composition during T1D progression
- Islet cells show changes in protein expression during T1D progression
- Immune cells are highly proliferative in T1D pancreata



Multiplexed *In Situ* Imaging Mass Cytometry Analysis of the Human Endocrine Pancreas and Immune System in Type 1 Diabetes

Yue J. Wang,¹ Daniel Traum,² Jonathan Schug,¹ Long Gao,¹ Chengyang Liu,³ HPAP Consortium,⁴ Mark A. Atkinson,⁵ Alvin C. Powers,⁶ Michael D. Feldman,⁷ Ali Naji,³ Kyong-Mi Chang,² and Klaus H. Kaestner^{1,8,*}

¹Department of Genetics and Institute for Diabetes, Obesity and Metabolism, Perelman School of Medicine, University of Pennsylvania, Philadelphia, PA 19104, USA

²Medical Research, Corporal Michael J. Crescenz Veterans Affairs Medical Center and Department of Medicine, Perelman School of Medicine, University of Pennsylvania, Philadelphia, PA 19104, USA

³Department of Surgery, Perelman School of Medicine, University of Pennsylvania, Philadelphia, PA 19104, USA

⁴Human Pancreas Analysis Program, <https://hpap.pmacs.upenn.edu/>

⁵Departments of Pathology and Pediatrics, University of Florida Diabetes Institute, Gainesville, FL 32610, USA

⁶Department of Medicine, Department of Molecular Physiology and Biophysics, Division of Diabetes, Endocrinology, and Metabolism, Vanderbilt University Medical Center VA, Tennessee Valley Healthcare, Nashville, TN, USA

⁷Department of Pathology, Perelman School of Medicine, University of Pennsylvania, Philadelphia, PA 19104, USA

⁸Lead Contact

*Correspondence: kaestner@pennmedicine.upenn.edu

<https://doi.org/10.1016/j.cmet.2019.01.003>

SUMMARY

The interaction between the immune system and endocrine cells in the pancreas is crucial for the initiation and progression of type 1 diabetes (T1D). Imaging mass cytometry (IMC) enables multiplexed assessment of the abundance and localization of more than 30 proteins on the same tissue section at 1-μm resolution. Herein, we have developed a panel of 33 antibodies that allows for the quantification of key cell types including pancreatic exocrine cells, islet cells, immune cells, and stromal components. We employed this panel to analyze 12 pancreata obtained from donors with clinically diagnosed T1D and 6 pancreata from non-diabetic controls. In the pancreata from donors with T1D, we simultaneously visualized significant alterations in islet architecture, endocrine cell composition, and immune cell presentation. Indeed, we demonstrate the utility of IMC to investigate complex events on the cellular level that will provide new insights on the pathophysiology of T1D.

INTRODUCTION

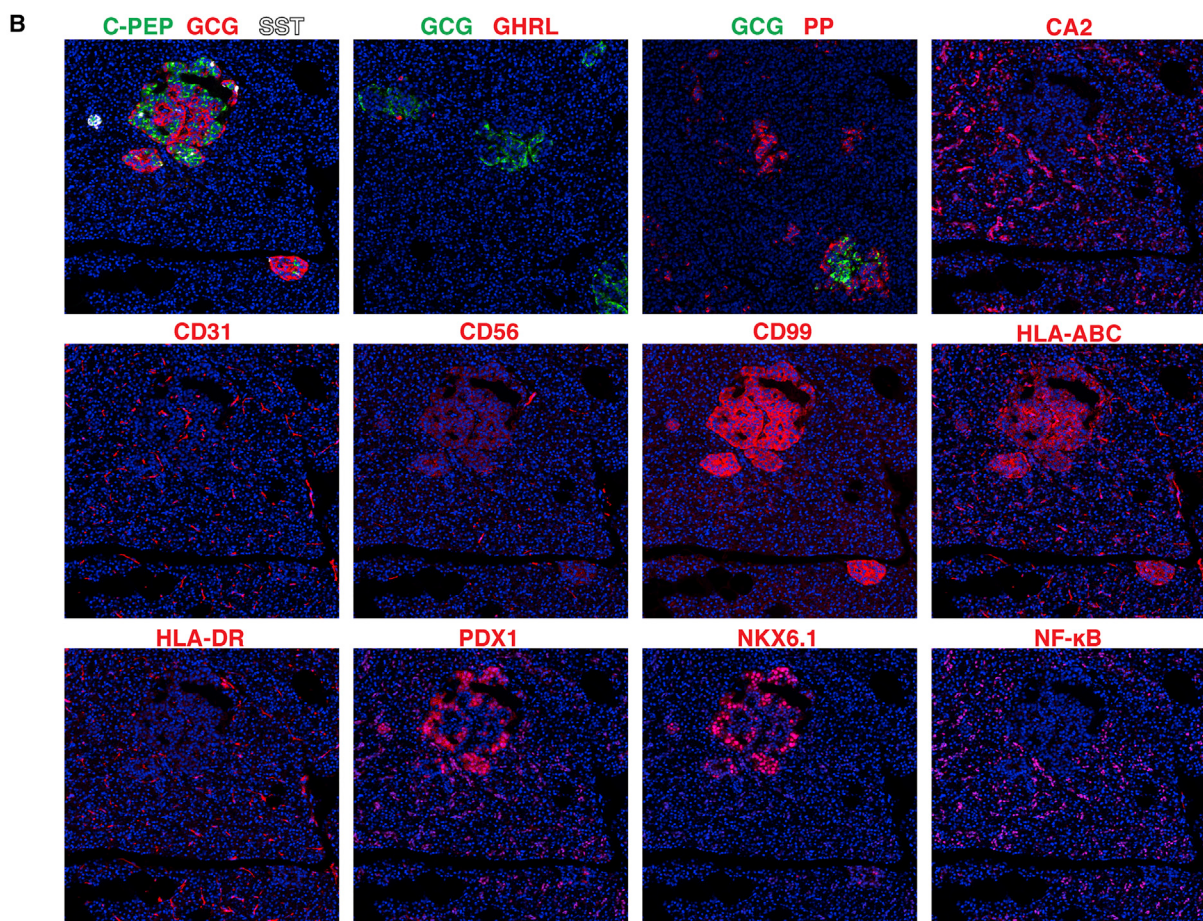
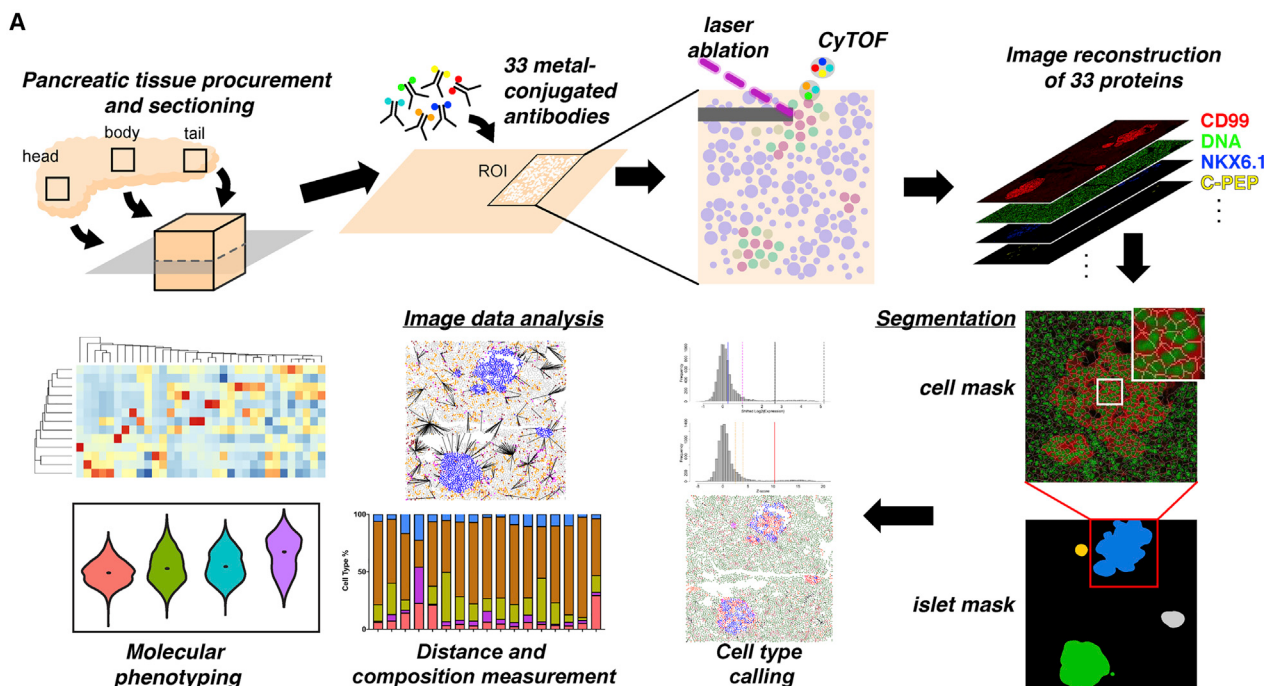
The pancreas is a highly complex organ consisting of multiple endocrine, exocrine, and stromal cell types and an intricate vascular and neuronal network. In the case of type 1 diabetes (T1D), bidirectional interactions between immune cells and insulin-producing beta cells lead to loss of functional pancreatic beta cell mass and a dependence on exogenous insulin administration for survival. Frequently, autoantibodies to beta cell antigens are present in the bloodstream months to years before the clin-

ical diagnosis of T1D (Pihoker et al., 2005). Decades of histopathology and molecular analyses, taken together with natural history studies, have suggested a model of T1D pathogenesis that includes genetic risk factors, chiefly driven by the human leukocyte antigen (HLA) loci, combined with an environmental “triggering event” such as a viral infection that eventually leads to beta cell autoimmunity (Atkinson and Eisenbarth, 2001; Atkinson, 2012). However, the etiology of the disease is still not completely understood.

Determining the sequential pathogenic events that take place in the T1D pancreas prior to the onset of hyperglycemia and in the months and years thereafter, is key to understanding the disease and derive effective therapeutic methods to halt the deterioration of pancreatic beta cells. However, the endeavor is severely hampered by the fact that the biopsy of pancreas—in contrast to the skin or colon—is not easily done (Atkinson, 2014; Mueller et al., 1988). Thus, investigations have focused on repeated sampling of blood for the identification and tracking of biomarkers ascribing evidence of immune dysregulation (such as the aforementioned autoantibodies), along with analysis of pancreatic tissue samples from deceased organ donors with T1D. Such tissue samples have been procured through organizations such as the Network for Pancreatic Organ donors with Diabetes (nPOD) (Campbell-Thompson et al., 2012) and more recently, the Human Pancreas Analysis Program (HPAP; <https://hpap.pmacs.upenn.edu/>). Nevertheless, tissue supply is extremely limited.

One major effort of modern histopathological studies using these precious pancreatic tissues is to glean as much information as possible for immune and islet cell subtyping, identification of cell-cell interactions, as well as other cellular phenotypes involved in T1D pathogenesis. One way to achieve this is by combinatorial immunolabeling and detection *in situ*. The information provided by multiplexed protein expression is not simply additive; rather, it can offer unique insights into the cellular states and complex biological functions executed by different cell types





(legend on next page)

within the microenvironment. To this goal, we adapted the recently developed and commercialized imaging mass cytometry (IMC) technology (Angelo et al., 2014; Chang et al., 2017; Giesen et al., 2014) for the analysis of human pancreata. In the IMC system, tissue slides are labeled with metal-conjugated antibodies. Post staining, the slides are ablated by a UV-laser spot-by-spot, and the resulting plumes of particles are carried over to a mass spectrometer for signal detection (Giesen et al., 2014). The precise laser registration in the sample ablation step allows for signal detection at 1- μm resolution. In addition, since the antibodies are conjugated with rare-earth metals not found in biological tissues, their signals have very low background (Angelo et al., 2014; Giesen et al., 2014). More importantly, the discrete time-of-flight measurement of isotope mass in the mass spectrometry instrument facilitates multiplexing. In the current work, we developed, validated, and utilized a panel of 33 antibodies, building on a panel we previously assembled for cell suspension mass cytometry (CyTOF; Wang et al., 2016). Our data demonstrate that IMC represents an innovative approach in the diabetes researcher's arsenal that will facilitate complex and nuanced investigations for a better understanding of the immune system-beta cell interactions that are critical to the pathogenesis of T1D.

RESULTS

Optimization of IMC in Human Pancreatic Tissue

With IMC, dozens of antibodies can be simultaneously employed to label tissue sections and their signals quantified with a single round of laser ablation (Giesen et al., 2014). For the current study, we sought to apply IMC to better understand the interactions between immune cells and pancreatic endocrine cells during the progression of T1D. Due to the superior morphology of formalin-fixed paraffin-embedded (FFPE) tissue sections, we optimized our staining protocol accordingly. We found that the majority of the antibodies tested showed optimal signal-to-noise ratios when antigen retrieval was performed at 95°C in a pH9.2 antigen retrieval buffer (Figures S1A and S1B; Tables S1–S3; see also STAR Methods). Our final panel consisted of 33 antibodies (Table S1) targeting all five endocrine cell types: beta cells (C-PEPTIDE [C-PEP], NKX6.1, and pancreatic and duodenal homeobox 1 [PDX1]), alpha cells (GLUCAGON [GCG]), delta cells (SOMATOSTATIN [SST] and PDX1), PP cells (pancreatic polypeptide [PP]), and epsilon cells (GHRELIN [GHRL]). We also included markers for pancreatic ductal and acinar cells (pan-keratin, CD44, PDX1, NKX6.1, carbonic anhydrase II [CA2], and pS6), endothelial and stromal cells (CD31 and NESTIN), the extracellular matrix (ECM; Collagen Type 1), and immune

cells of the myeloid as well as lymphoid lineages: all (CD45); B cells (CD20); T cells (CD3, CD4, and CD8); memory T cells (CD45RO); Tregs (FOXP3); macrophages/dendritic cells (CD68, CD14, CD11b, and HLA-DR); NK cells (CD56 and CD57); cytolytic granules (Granzyme B [Gnzb]); and antigen presentation (HLA-ABC and HLA-DR). Nuclear factor κ B (NF- κ B) was included initially to monitor immune responses. Subsequently, we found that this protein was constitutively expressed in the nuclei of pancreatic ductal cells (Figure 1B, last panel). A similar expression pattern for NF- κ B has been described in the zebrafish pancreas (Wang et al., 2015). Finally, we employed beta-actin and CD99 as ubiquitous cell markers and Ki67 as a proliferation marker.

For our study of the disease duration-dependent changes in immune cell-endocrine cell cross-talk, we selected tissues from 18 donors available from the nPOD and HPAP tissue collections (Table S4). Among these 18 donors, six were controls with no history of diabetes, and 12 were donors with T1D. The donors with T1D were separated into three groups, with three to five donors each, based on the time since diagnosis: \leq 2-year diabetes duration (T1D \leq 2; n = 4); 5- to 11-year diabetes duration (T1D \leq 11; n = 5); and \geq 21-year duration (T1D \geq 21; n = 3). Donors were matched by age, sex, race/ethnicity, and BMI. We sampled one slide each from the head, body, and tail of the pancreata for all donors except NPOD6367, where tissue was only available from the head and tail of the pancreas (Table S4). Our experimental outline is shown in Figure 1A. Representative antibody labeling patterns are shown in Figures 1B and S1B. For sample acquisition, we first identified islets based on the bright-field image acquired prior to tissue ablation and then, selected surrounding regions of interest (ROIs) with the approximate size of 1,000 $\mu\text{m} \times 1,000 \mu\text{m}$. We acquired 196 ROIs (three to eight per slide) containing a total of 2,191 islets from 18 donors, with an average of 122 ± 47 islets per donor.

Image Data Processing and Cell-Type Calling

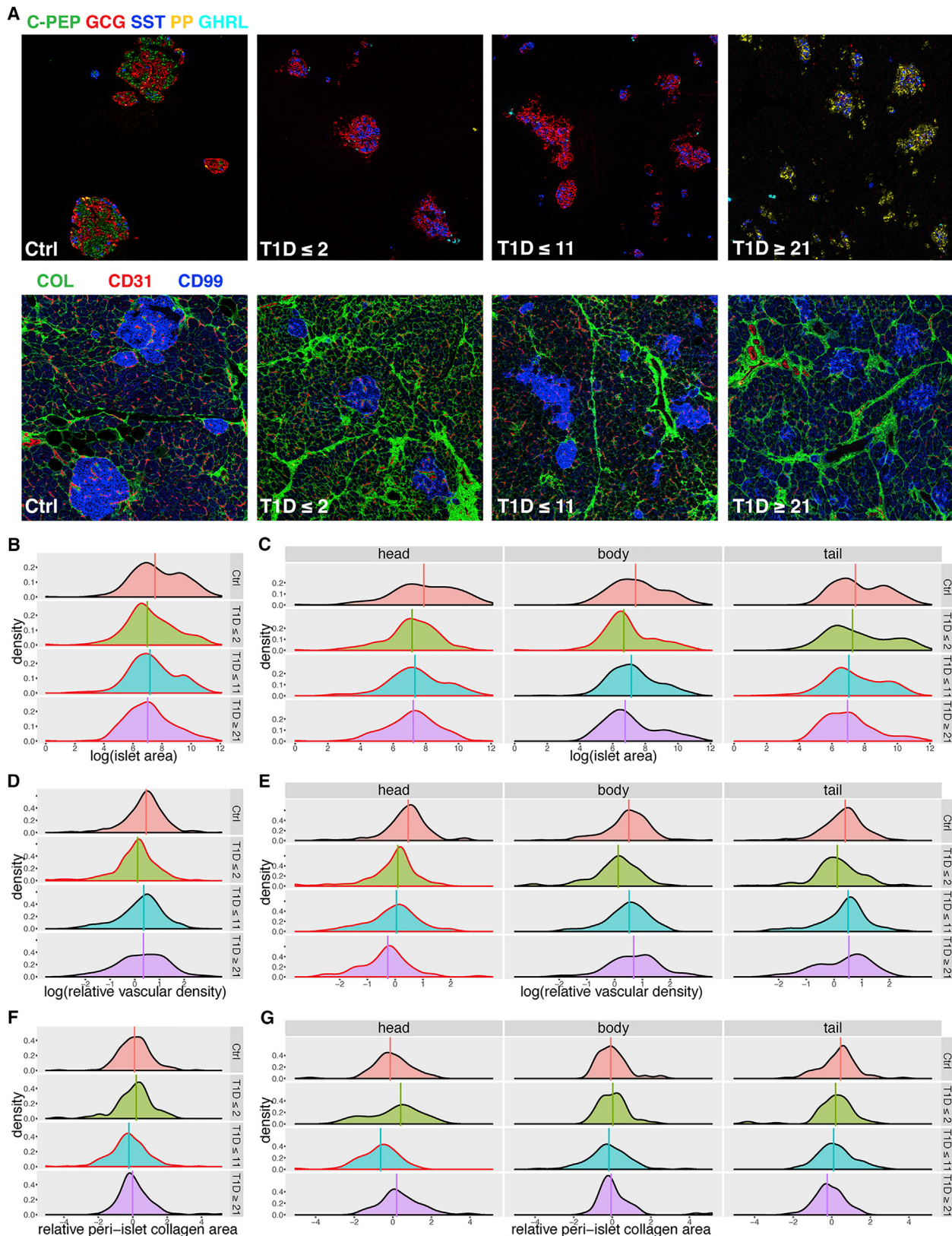
As the first step of imaging processing, we performed pixel-level compensations to mitigate the low-level spillovers observed between a given detection channel, its neighboring channels, and the channels containing potential oxidation products, followed by “hot pixel” removal (Figure S2A; STAR Methods). We then segmented each raw image into islets and individual cells, based on the summation of endocrine marker staining for the former and DNA plus membrane staining for the latter (Figures 1A and S2B–S2D). The islet mask was used for downstream islet structural analyses, including islet size measurement, intra-islet vasculature density assessment, and peri-islet ECM quantification. Due to the geometry and staining differences of pancreatic

Figure 1. Workflow and Antibody Validation for Imaging Mass Cytometry Study of the Human Pancreas

(A) Schema of the experimental platform. 4- to 8- μm FFPE sections of human pancreatic tissues are labeled simultaneously with 33 metal conjugated antibodies. 1,000 $\mu\text{m} \times 1,000 \mu\text{m}$ regions of interest (ROIs) around islets are selected for laser ablation. Plumes of particles are carried over to CyTOF for signal quantification. Antibody labeling patterns are reconstructed and output as 32-bit images. Islet-level and cell-level segmentation are performed to enable downstream image analyses.

(B) Staining patterns of the newly developed metal-conjugated antibodies confirm their specificity. Displayed channels for each panel from top to bottom, left to right are: C-PEP (green)/GCG (red)/SST(white), GCG (green)/GHRL (red), GCG (green)/PP (red), CA2 (red), CD31 (red), CD56 (red), CD99 (red), HLA-ABC (red), HLA-DR (red), PDX1 (red), NKX6.1 (red), and NF- κ B (red). Iridium-DNA staining is shown in blue in all panels. All panels are from the same ROI except GCG/GHRL and GCG/PP panels.

See also Figures S1–S3 and Tables S1–S5.



(legend on next page)

parenchymal cells and immune cells, separate cell masks were constructed for each population (Figures S2C and S2D). These masks were carried into the cell-type calling pipeline and formed the basis for our cell-level analyses.

To identify positive signals for different proteins, we combined automatic thresholding based on a Gaussian model to decompose signal intensities, together with manual curation aided by Gaussian mixture models to identify positive and negative cutoffs for each individual channel (Figures S2C and S2D; see **STAR Methods** for details). Combinatorial Boolean rules for each cell type were then applied to assign cells to their corresponding cell types (Table S5; **STAR Methods**). The cell-type calling results from the algorithm aligned with visual inspection and agreed with manual gating (Figures S2C–S2F). In addition, the automated cell-type calling was insensitive to cell masks generated independently by two different investigators (Figures S2G and S2H).

To verify our cell-type calling result further, we grouped all cells based on their cell-type annotations and used the heatmap with hierarchical clustering to visualize their mean relative expression levels (Figure S3A). As expected, each cell type exhibited its canonical marker expression profile (Figure S3A). As a further cross-validation of our system, we quantified the endocrine cell composition from IMC data acquired from two of the HPAP donors (Figures S3B–S3D). In parallel, endocrine cell percentages from the same two donors were quantified by CyTOF from single-cell suspensions, following the same procedure as we have established previously (Wang et al., 2016). A minimum of 7,000 endocrine cells were quantified with CyTOF and IMC for both donors. The signal patterns of marker channels and the quantification of all five endocrine cell types between these two systems were similar, as expected (Figures S3B–S3D). The slight differences in cell-type frequencies could be explained by differences in the sampling method: for CyTOF, islets isolated

from the whole pancreas are randomly sampled, while for IMC, only the islets present in the imaged ROIs are analyzed.

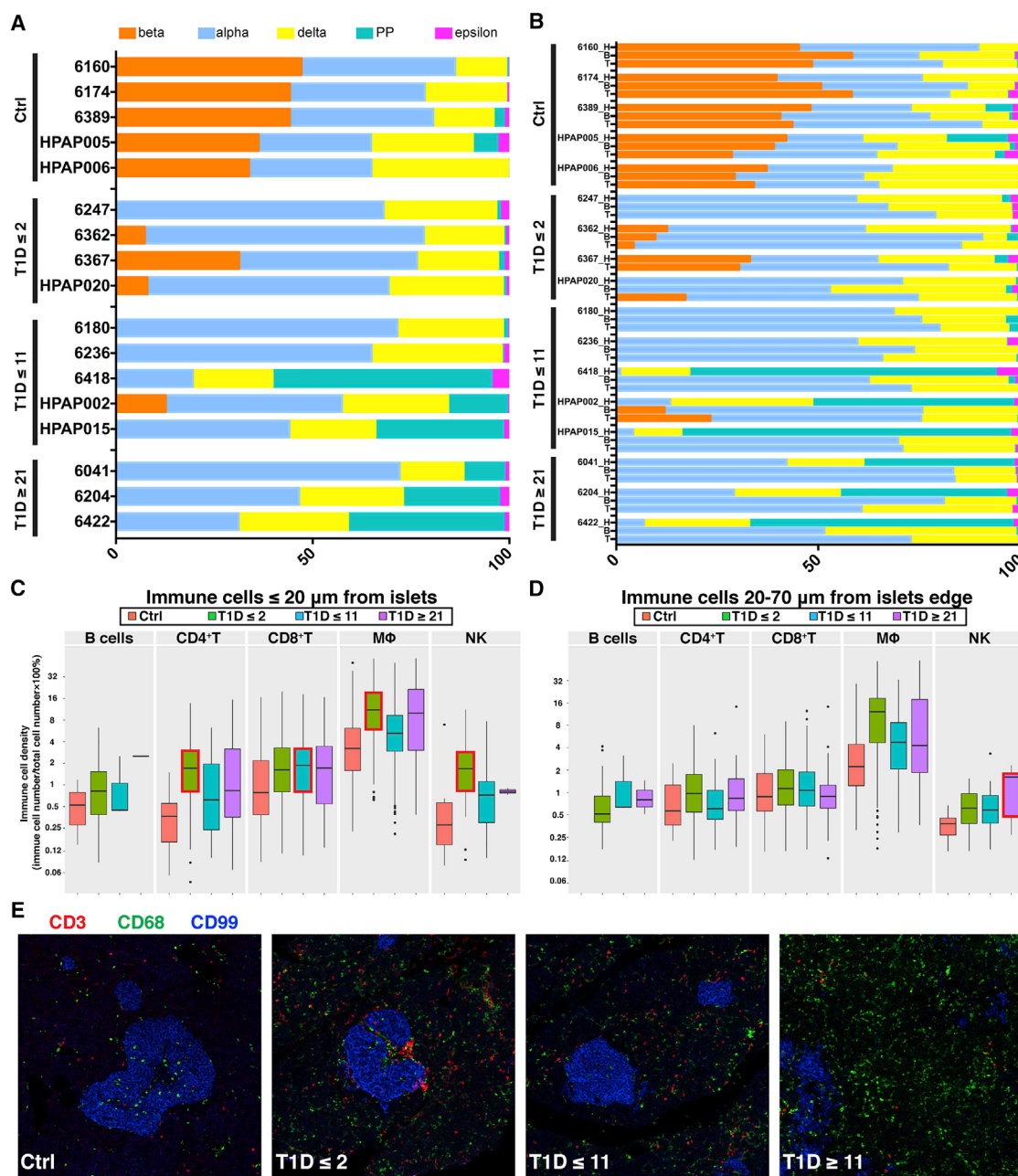
During image processing, we observed a high density of collagen and immune cells in images from the non-diabetic control donor HPAP014 (a 43-year-old Caucasian female with no history of diabetes), and on further inspection, we found morphological changes in the pancreatic acinar cells suggestive of pancreatitis, though pancreatitis had not been diagnosed clinically. IMC data from this donor further indicated that several regions displayed pancreatic intraepithelial neoplasia (PanIN), which is characterized by duct hyperplasia with columnar epithelial cells and concomitant acinar cell atrophy. The endocrine tissue appeared to be spared at this stage of the disease (data not shown). The complete encasement of islets by collagen and their parallel blood supply may buffer them from damaging local signals (Lifson et al., 1980; and discussed further below). Because of this observed pathology, this donor was excluded from further analysis.

Islet Structural Changes during T1D Progression

First, we quantified the morphological features of islets and examined whether they were altered in donors with different durations of disease. We noticed that islet areas were reduced and that islets showed a “ragged” morphology in patients with T1D, including in those with recent onset of disease (Figure 2A). The reduction in islet size in all groups of T1D donors compared with controls was significant after controlling for individual donor effect (linear mixed-effects model test, $p \leq 0.05$) (Figure 2B). This is in line with the notion that by the time T1D clinically manifests, the pancreas has already undergone substantial structural and functional changes associated with extensive loss of beta cell mass and function (Atkinson and Eisenbarth, 2001; Atkinson et al., 2014; Eisenbarth, 1986). Considering the potential regional heterogeneity of islet distribution (Wang et al., 2013), we next

Figure 2. Architectural Changes in Islets of T1D Donors

- (A) Selected channel overlays for control donors and donors with different T1D durations. Islets from donors with T1D are smaller and exhibit rugged appearance (top panels). The ECM and vascular labeling of the same ROI is also shown (bottom panels). Displayed channels are as follows: top, C-PEP (green), GCG (red), SST (blue), PP (yellow), and GHRL (cyan); bottom, type 1 collagen (COL, green), CD31 (red), and CD99 (blue).
- (B–G) Islet-level quantifications for all pancreatic regions combined (B, D, and F) or stratified by head, body, and tail parts of the pancreata (C, E, and G). Individual islet measurements are used as input. Curves with a red outline indicate statistical significance compared to non-diabetic controls with a p value ≤ 0.05 . Tests for linear mixed-effects models are used for all statistical analyses. The vertical line from each plot represents population median.
- (B) Islet sizes are significantly reduced in patients with T1D regardless of disease duration. Density distributions of islet areas are shown in natural logarithm scale. Statistics are calculated with the area of islets in log scale as response and donor types (Ctrl, T1D ≤ 2 , T1D ≤ 11 , and T1D ≥ 21) as categorical predictor. Individual donor effect is adjusted as a random effect. Numbers of islets used for the analysis are $n = 465$ in control group, $n = 500$ in T1D ≤ 2 group, $n = 641$ in T1D ≤ 11 group, and $n = 468$ in T1D ≥ 21 group.
- (C) Islet size quantification by anatomic locations. Statistics are calculated separately for the head, body, and tail regions of the pancreata following as in Figure 2B. Numbers of islets used for the analysis are head, $n = 140$ in control group, $n = 184$ in T1D ≤ 2 group, $n = 239$ in T1D ≤ 11 group, and $n = 183$ in T1D ≥ 21 group; body, $n = 154$ in control group, $n = 164$ in T1D ≤ 2 group, $n = 235$ in T1D ≤ 11 group, and $n = 132$ in T1D ≥ 21 group; tail, $n = 171$ in control group, $n = 152$ in T1D ≤ 2 group, $n = 167$ in T1D ≤ 11 group, and $n = 153$ in T1D ≥ 21 group.
- (D) Intra-islet vascular density is significantly reduced in donors with recent-onset diabetes (T1D ≤ 2). Density of intra-islet vasculature is normalized to the vascular density of the exocrine tissue of the same ROI. Statistics are calculated as in Figure 2B, except that the relative vascular density in log scale is used as the response variable. Numbers of islets used for the analysis are the same as in Figure 2B.
- (E) Intra-islet vascular density is reduced in the head region of the pancreata for all T1D donors. Statistics are calculated separately for different regions as in Figure 2D. Numbers of islets used for the analysis are the same as in Figure 2C.
- (F) Peri-islet collagen density is reduced in patients with medium duration of diabetes (T1D ≤ 11). Statistics are calculated as in Figure 2B, except that the relative collagen area (collagen area divided by the corresponding islet peripheral area) is logit transformed and used as the response variable. Numbers of islets used for the analysis are the same as in Figure 2B.
- (G) Peri-islet collagen density is reduced specifically in the head region of pancreata from patients with median duration of diabetes (T2D ≤ 11). Statistics are calculated separately for different regions of the pancreas as in Figure 2F. Numbers of islets used for the analysis are the same as in Figure 2C.
- See also Figure S4.

**Figure 3. Census of Endocrine and Immune Cell Composition in the Human Pancreata**

(A) Quantification of the proportions of endocrine cell types for each donor. Numbers of endocrine cells in each ROI used for the analyses are shown in [Table S6](#). A linear mixed-effects model is used for statistical testing with logit transformed cell proportion as the response and donor types as the predictor. Individual donor effect is adjusted as a random effect, with $p \leq 0.05$ as the significant cutoff. Comparisons that reach statistical significance include: the proportion of beta cells in all T1D donors are significantly reduced compared with controls, the proportion of alpha cells is significantly increased in T1D ≤ 2 donors compared with controls, and the proportions of PP cells in T1D ≤ 11 and T1D ≥ 21 groups are significantly increased compared with controls.

(B) Quantification of the proportions of endocrine cell types for each donor stratified by different regions of the pancreata. Numbers of endocrine cells in each ROI used for the analyses are shown in [Table S6](#). A linear mixed-effects model is used for statistical testing with logit transformed cell proportion as the response and donor types together with tissue parts as predictors. Individual donor effect is adjusted as a random effect, and $p \leq 0.05$ is used as the significant cutoff. Comparisons that reach statistical significance include: proportion of beta cells in the head is significantly reduced compared with body and tail parts of the pancreata; proportion of alpha cells in the head is significantly reduced compared with body and tail parts of the pancreata, and proportion of PP cells in the head is significantly increased compared with body and tail parts.

(C) Quantification of immune cells inside or within 20 μm from the edge of islets. Cell numbers are normalized to the total numbers of cells (immune + non-immune) in the same area. Measurements from individual islets are used as input and listed in [Table S6](#). Boxplots with red outlines indicate significant cell density differences between T1D donors compared to controls. Statistical analyses are performed by linear mixed-effects model with logit transformed cell density as the response and donor types as predictor, with $p \leq 0.05$ as the significant cutoff.

(legend continued on next page)

stratified our comparisons into pancreatic head, body, and tail regions. Compared with controls, we found a significant reduction of islet size in the head region of the pancreata from all T1D donor groups (linear mixed-effects model test, $p \leq 0.05$) (Figure 2C, left panel). In pancreas body, islet size was only significantly reduced in the $T1D \leq 2$ donor group compared with controls (linear mixed-effects model test, $p \leq 0.05$) (Figure 2C, middle panel). In contrast, in both the $T1D \leq 11$ and $T1D \geq 21$ donor groups, islets were smaller in the tail region of the pancreata compared to controls (linear mixed-effects model test, $p \leq 0.05$) (Figure 2C, right panel). Our results differ from a previous report where smaller islets were observed in all regions of the pancreas in two donors with T1D (Poudel et al., 2015). Differences in patient cohorts and the well-recognized heterogeneity of histological changes that occur in T1D likely underlie this discrepancy.

Pancreatic islets are highly vascularized (Bonner-Weir and Orci, 1982). However, the status of islet vascularization during the progression of T1D is not known. To assess the changes of intra-islet vascular density, we measured the ratio of intra-islet endothelial area to islet area normalized against the vascular density in the exocrine tissue of the same ROI. We observed a significant reduction of vascular area in $T1D \leq 2$ donors compared to controls (linear mixed-effects model test, $p \leq 0.05$) (Figure 2D). Region-specific analysis revealed that the vascular density was significantly reduced specifically in the head of the pancreas in all T1D donor groups compared with controls (linear mixed-effects model test, $p \leq 0.05$) (Figure 2E).

Changes to the ECM, including loss of basement membrane and interstitial matrix integrity, have been implicated in the pathogenesis of T1D (Bogdani et al., 2014; Korpos et al., 2013). Therefore, we investigated the extent of peri-islet ECM degradation by analyzing type 1 collagen abundance and distribution. In the control tissues, the majority of islets were surrounded by collagen. In contrast, the collagen capsule was fragmented around islets from donors with T1D (Figure 2A, bottom panel). When we quantified the peri-islet area covered by collagen, we found a significant reduction in $T1D \leq 11$ donors but not from $T1D \leq 2$ or $T1D \geq 21$ donors (linear mixed-effects model test, $p \leq 0.05$) (Figure 2F). This observation aligns with previous reports indicating early destruction and later rebuilding of the ECM around T1D islets (Bogdani et al., 2014; Korpos et al., 2013). Moreover, when comparing islets from the head, body, and tail regions of the pancreata, only the islets in the pancreas head from the $T1D \leq 11$ group showed reduction in their peri-islet collagen compared with control islets (linear mixed-effects model test, $p \leq 0.05$) (Figure 2G).

To estimate the dependency of vascular density and peri-islet collagen area on islet size, we performed regression analyses (Figure S4). We found that only in the $T1D \geq 21$ donor group, there were mild but significant trends of reduced vascular densities and reduced peri-islet collagen areas with bigger islets (linear regression t test, $p \leq 0.05$) (Figure S4). Reduced islet

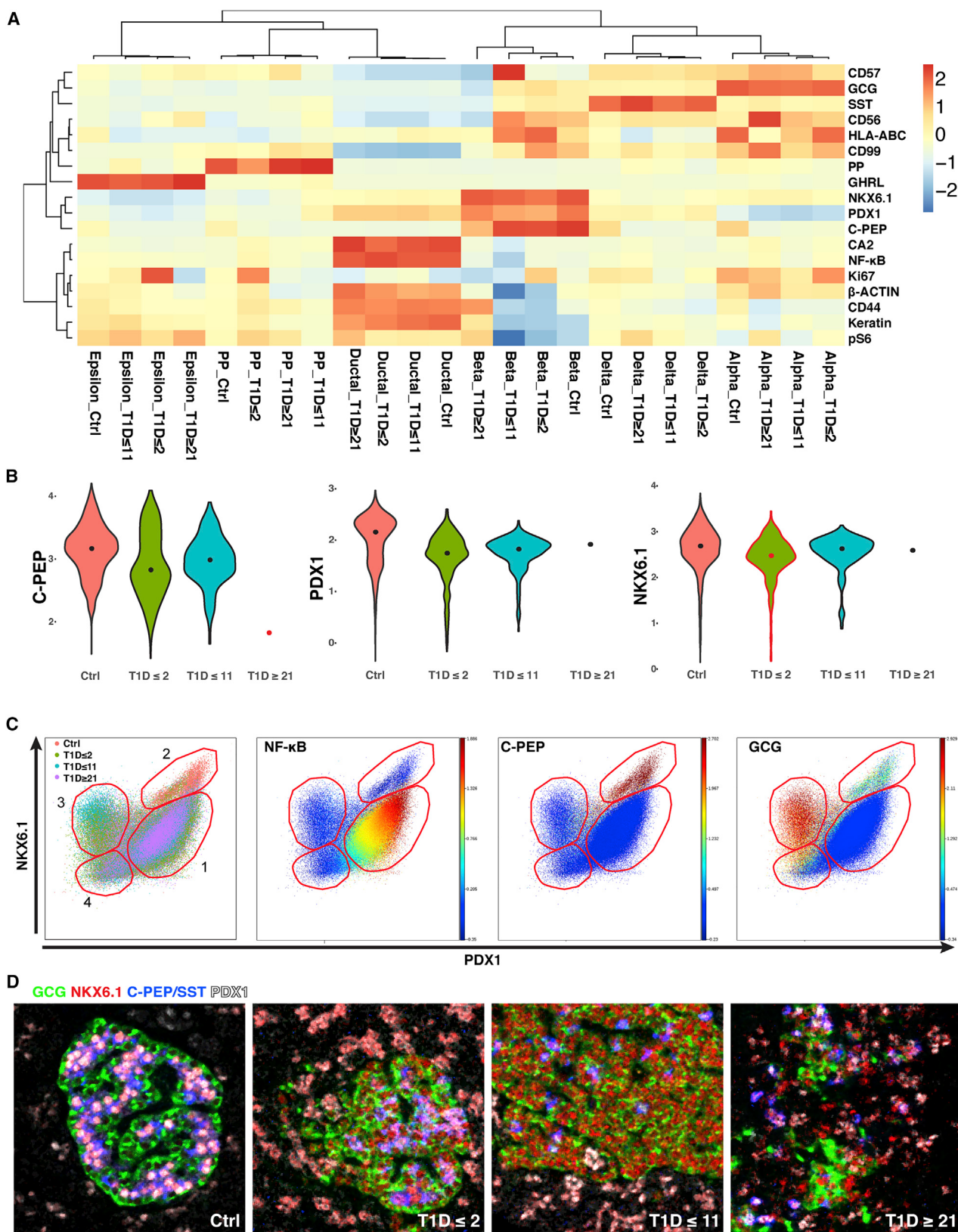
perfusion and structural integrity in larger islets from donors with long duration diabetes may indicate a failure of adaptation and may contribute to the selective elimination of larger islets in patients with longer duration T1D.

Alterations in Endocrine and Immune Cell Compositions in T1D Pancreata

Next, we quantified the proportions of endocrine cells in donor pancreata. As expected, compared with control donors, all donors with T1D exhibited a significantly reduced percentage of beta cells (linear mixed-effects model test, $p \leq 0.05$) (Figure 3A; Table S6). The proportion of beta cells was positively correlated with C-PEPTIDE levels in the donors' blood samples (linear regression t test, $p < 0.05$) (Figure S5). Conversely, the alpha cell fraction was increased in all T1D donors compared with controls, although statistical significance was only reached in the $T1D \leq 2$ donor group (linear mixed-effects model test, $p \leq 0.05$) (Figure 3A; Table S6). In addition, there was a significant increase in the PP cell percentage in the $T1D \leq 11$ and $T1D \geq 21$ donor groups compared to controls (linear mixed-effects model test, $p \leq 0.05$) (Figures 2A and 3A; Table S6). PP cells are highly concentrated in a small region from the head of the pancreas called the uncinate lobe (Malaisse-Lagae et al., 1979; Stefan et al., 1982). Indeed, our data confirmed that the head region of the pancreas had a significantly higher percentage of PP+ cells compared with the body and tail regions (linear mixed-effects model test, $p \leq 0.05$) (Figure 3B; Table S6). In contrast, both beta and alpha cell percentages were lower in the head compared with the body and the tail regions (linear mixed-effects model test, $p \leq 0.05$) (Figure 3B; Table S6).

Previous work has shown that immune cell abundance within the islets fluctuates with duration of T1D (Willcox et al., 2009). We quantified five major immune cell subsets, including B cells, CD4⁺ T cells, CD8⁺ T cells, macrophages, and NK cells in the pancreatic sections from all donors grouped by disease duration. Immune cell density was determined for two separated regions associated with each islet: islets plus the halo extending 20 μm from the islet edge (proximal region) (Figure 3C) or in the area extending 20–70 μm from the islet perimeter into the exocrine pancreas (distal region) (Figure 3D). Overall, immune cell density was higher in the proximal region compared to the distal region, but both regions displayed similar immune cell representations (Figures 3C and 3D; Table S6). Macrophages were the predominant immune cells present in both the control and T1D human pancreas (Figures 3C–3E; Table S6). On the other hand, B cells and NK cells were generally of low abundance in all pancreatic tissues examined (Figures 3C–3E; Table S6). In the proximal region, densities of CD4⁺ T cells, macrophages, and NK cells were significantly increased in the $T1D \leq 2$ donor group compared with controls (linear mixed-effects model test, $p \leq 0.05$) (Figure 3C). CD8⁺ T cells were also significantly enriched in the $T1D \leq 11$ donors compared with controls (linear mixed-effects model test, $p \leq 0.05$) (Figure 3C). In the distal

(D) Quantification of immune cells 20–70 μm distal to islets. Measurements from individual islets are used as input and listed in Table S6. Boxplots with red outlines indicate significant cell density difference among T1D donors compared to controls. Statistical analysis is the same as in Figure 3C.
 (E) Representative IMC images exhibit immune cell presentation in control and T1D donors. Displayed channels are: CD3 (red), CD68 (green), and CD99 (blue). See also Figure S5 and Table S6.



(legend on next page)

region, NK cell numbers were significantly increased in the T1D ≥ 21 donor group compared with controls (linear mixed-effects model test, $p \leq 0.05$) (Figure 3D). The different kinetics and spatial distribution of immune cell profiles support their different roles during the pathogenesis of T1D (Phillips et al., 2009).

Molecular Changes in T1D Pancreata

Next, we took advantage of the cellular resolution and quantitative nature of IMC to determine expression changes at the protein level in different cell types in the T1D pancreata. Due to the difference in protein expression profiles, we separated the analyses of pancreatic epithelial cells from those of immune cells.

Recently, several studies have reported on the presence of double hormone-positive cells in the human pancreas (Spijkervet et al., 2015; Xin et al., 2016). In our system, ~4% of pancreatic epithelial cells were detected as polyhormonal. However, due to the limited 1- μm X-Y resolution of the IMC instrument and the fact that the entire tissue section was laser ablated, resulting in a Z resolution of 4–8 μm (the tissue section thickness), we could not distinguish true polyhormonal cells from “stacked” endocrine cells. Therefore, these cells with conflicted hormone expression were filtered out from our analysis. In addition, acinar cells were excluded from the current analyses due to the lack of specific markers for this cell type in our antibody panel.

We performed hierarchical clustering for pancreatic epithelial cells in each donor type based on their mean protein expression values. All cell types clustered as expected regardless of donor group (Figure 4A). Next, we focused our attention on three proteins: C-PEP, PDX1, and NKX6.1 and measured their relative levels in the beta cells (Figure 4B). C-PEP is a polypeptide derived from enzymatically cleaved proinsulin during the maturation of insulin (Asadi et al., 2015). PDX1 and NKX6.1 are two transcription factors that are important for pancreatic endocrine cell differentiation and function (Gu et al., 2002; Schaffer et al., 2013). There was large inter-donor heterogeneity in the levels of C-PEP, PDX1, and NKX6.1 in beta cells, and only the expression of NKX6.1 in the T1D ≤ 2 donor group was significantly lower compared with controls (linear mixed-effects model test, $p \leq 0.05$) (Figures 4B and S6A). We identified one remaining C-pep-

tide-positive beta cell in one of the T1D ≥ 21 donors (NPOD6422) (Figure S6B). This beta cell had significantly reduced C-PEP level, but NKX6.1 and PDX1 expression were maintained (linear mixed-effects model test, $p \leq 0.05$) (Figures 4B and S6).

When plotting the expression of PDX1 and NKX6.1 for all epithelial cells being analyzed, four populations could be discerned (Figure 4C). Population 1 had intermediate levels of PDX1 and NKX6.1 expression (Figure 4C, left panel); this population was also characterized by high levels of ductal marker expression, such as NF- κ B, indicating that they were likely ductal epithelial cells (Figure 4C, middle-left panel). Population 2 had the highest levels of PDX1 and NKX6.1 expression (Figure 4C, left panel) and also exhibited the highest C-PEP signal and thus, encompassed beta cells (Figure 4C, middle-right panel). Population 4 consisted of PDX1/NKX6.1 double-negative cells and contained GCG high-expressing alpha cells along with other epithelial cells (Figure 4C, left and right panel). Population 3 had intermediate NKX6.1 but was negative for PDX1 expression (Figure 4C, left panel). Surprisingly, this population also exhibited high GCG expression, suggesting an alpha cell phenotype (Figure 4C, right panel). This population was highly enriched for cells from T1D donors (Figure 4C, left panel). We referred back to the original IMC data and confirmed the presence of low-level NKX6.1 expression in alpha cells in T1D samples (Figure 4D). These data echo recent findings by Brissova and colleagues that documented the emergence of NKX6.1-expressing alpha cells in the T1D pancreas (Brissova et al., 2018). Defective glucagon secretion in response to hypoglycemia was noted in diabetes patients as early as 1973, suggesting an intrinsic alpha cell defect (Gerich et al., 1973). Due to the lack of longitudinal data from human samples, we could not distinguish whether these cells were derived from dysregulated alpha cells or dedifferentiated beta cells.

Similar to pancreatic epithelial cells, immune cells from different donors clustered by their cell types (Figure 5A). In particular, CD4 $^+$ T cells from the T1D ≥ 21 donor group exhibited the highest Ki67 expression (Figure 5A, black box). We next gated on the histogram of Ki67 and derived the percentage of Ki67 $^+$ cells in each cell type separated by each donor group

Figure 4. Quantification of Protein Expressions at the Cellular Level in the Human Pancreas

(A) Heatmap demonstrates that endocrine cells from different donors cluster by their cell types and display canonical marker expression. Input data are mean levels of each protein in each cell type for each donor type. Values associated with each row of the heatmap are centered and standardized separately. Heatmap color indicates Z score.

(B) Violin plots summarize the relative expressions of C-PEP (left panel), PDX1 (middle panel), and NKX6.1 (right panel) in the beta cells from different donors. Measurements from individual beta cells are used as input. The dot inside each violin represents the location of the population median for Ctrl, T1D ≤ 2 , and T1D ≤ 11 groups and the expression of the one beta cell in the T1D ≥ 21 group. Red outlines indicate statistical significance, tested by linear mixed-effects model with individual protein expression as the response and donor types as predictor. Individual donor effect is adjusted as a random effect, and $p \leq 0.05$ is set as the significant cutoff.

(C) Scatterplots display PDX1 versus NKX6.1 expression for all pancreatic endocrine and ductal cells. Each dot represents one cell. The same scatterplot is color coded by donor types: (left panel), NF- κ B expression (middle-left panel), C-PEP expression (middle-right panel), and GCG expression (right panel). Four populations emerge based on different levels of PDX1 and NKX6.1 expression. Left panel, group 2 is enriched for cells from control donors (coral dots); while group 3 is enriched for cells from T1D donors (green, turquoise, and violet dots for cells from T1D ≤ 2 , T1D ≤ 11 , and T1D ≥ 21 groups, correspondingly). Middle-left panel, ductal cells are located in group 1 and are characterized by high NF- κ B expression. Middle-right panel, beta cells are located in group 2 and have high C-PEP levels. Right panel, group 3 cells have high GCG levels, indicating their alpha-cell identity. Some of the alpha cells (identified by high GCG expression) also extend into group 4 regions.

(D) IMC data confirm the ectopic expression of NKX6.1 in alpha cells from T1D donors. Displayed channels are as follows: GCG (green); NKX6.1 (red); C-PEP, and SST (blue); PDX1 (white). The levels of NKX6.1 and PDX1 are separately adjusted for visualization in the control panel because of the significantly higher signals of these two channels in the islets from control donors. All panels are shown at 4X magnification.

See also Figure S6.

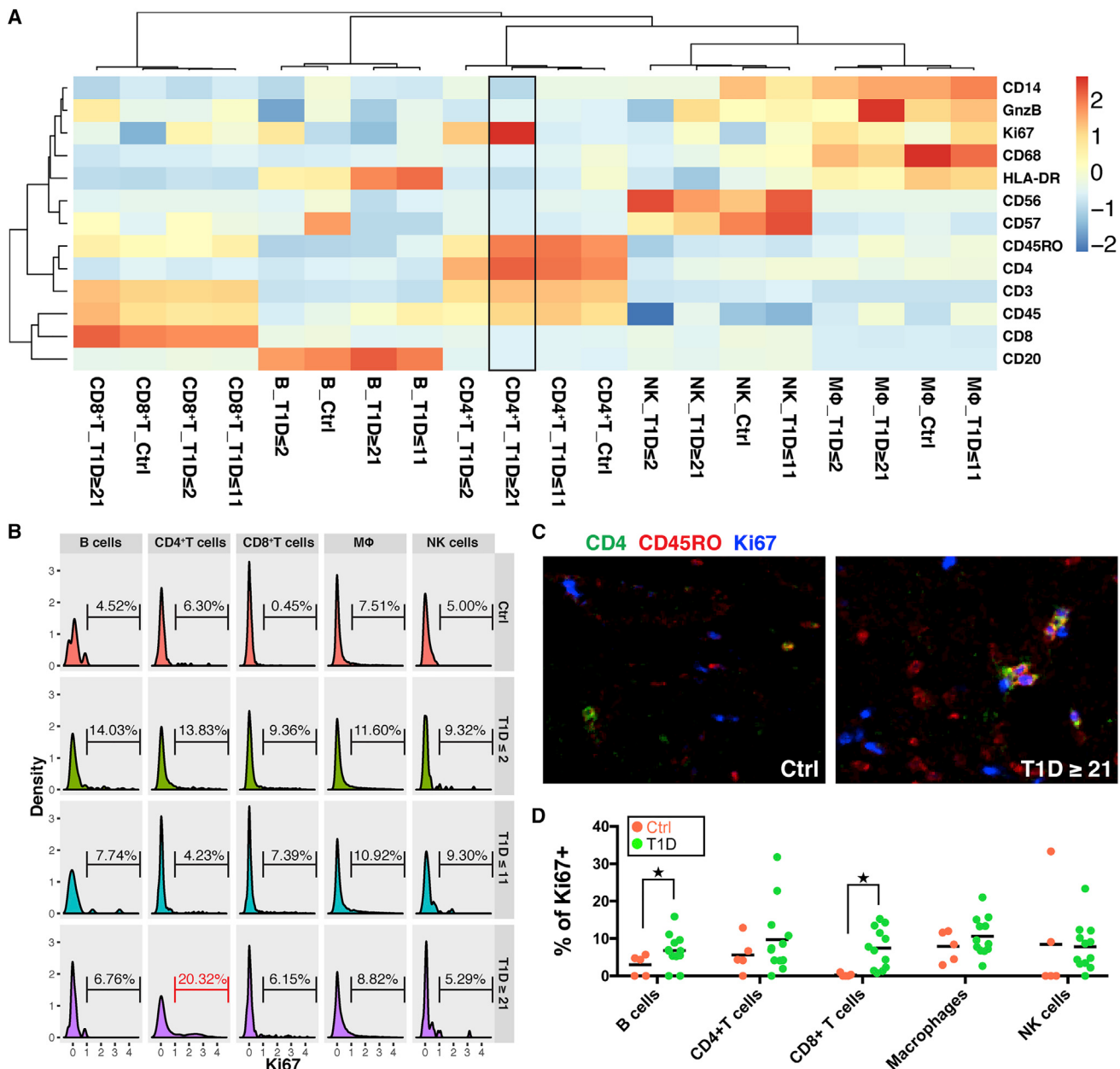


Figure 5. Quantification of Protein Expressions in Immune Cells in the T1D Pancreas

(A) Heatmap demonstrates that immune cells from different donors cluster by cell type and display canonical marker expression. CD4⁺T cells from patients with long duration diabetes (T1D ≥ 21) have high Ki67 level (black box). Input data are mean levels of each protein in each cell type for each donor type. Values associated with each row of the heatmap are centered and standardized separately. Heatmap color indicates Z score.

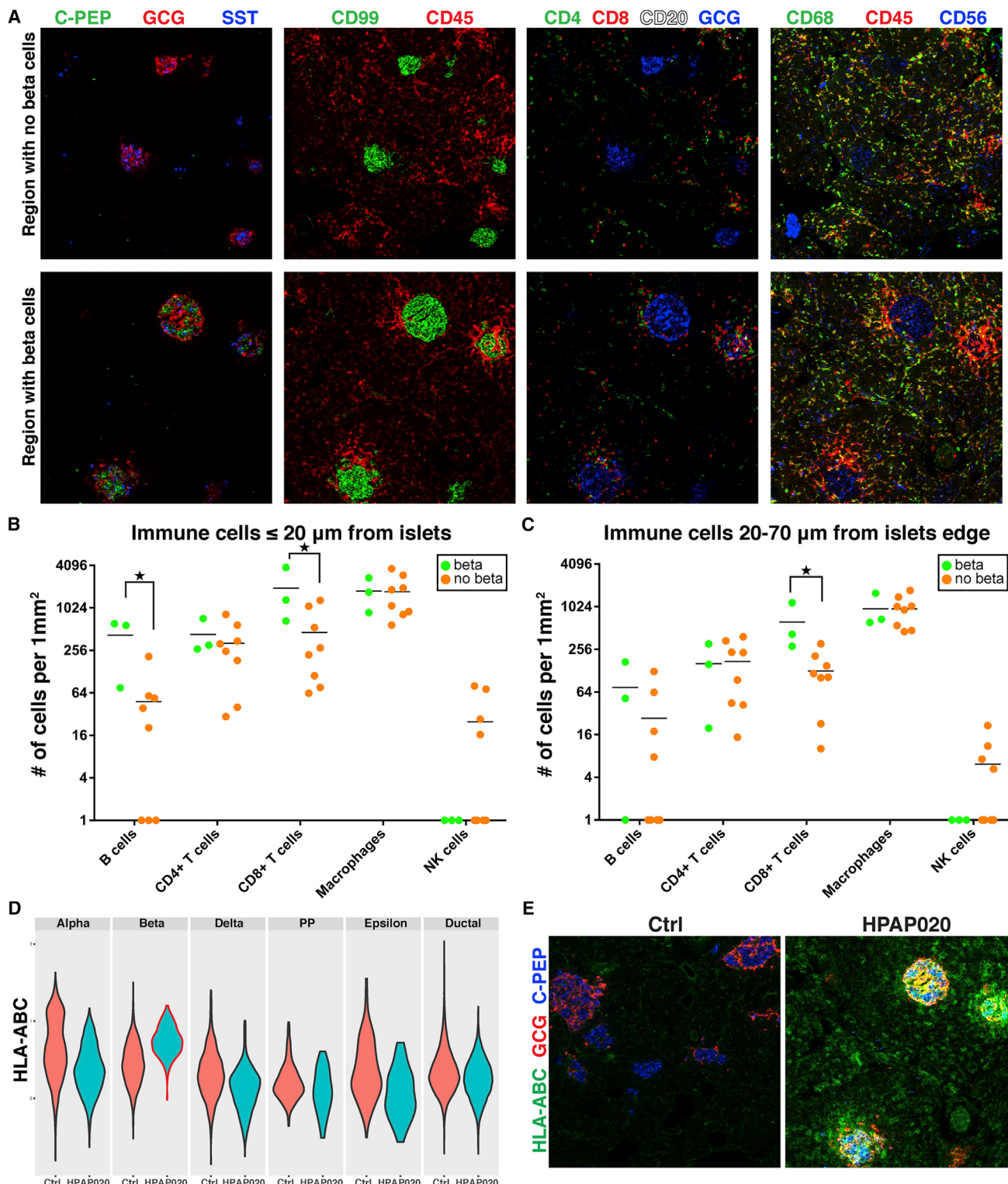
(B) Percentage of Ki67⁺ cells in each cell type of different donor groups. CD4⁺T cells from T1D ≥ 21 donors have the highest percentage of Ki67⁺ cells (red bracket). Ki67 values from each immune cell type for each donor type are used as input.

(C) Proliferating CD4⁺T cells in the long duration diabetes donor (T1D ≥ 21) display a memory phenotype. Displayed channels are as follows: CD4 (green), CD45RO (red), and Ki67 (blue). All panels are shown at 5× magnification.

(D) Quantification of percentage of proliferating cells in control and T1D donors. B cells and CD8⁺T cells show increased proliferation compared with controls. Each dot represents one donor. ★ indicates statistical significance based on Mann-Whitney test with p ≤ 0.05.

(Figure 5B). The histogram again showed that the highest percentage of Ki67⁺CD4⁺T cells was present in the T1D ≥ 21 donor group (Figure 5B, red bracket). In addition, these proliferating CD4⁺T cells were CD45RO high, indicating an activated memory

T cell phenotype (Figure 5C). The role of these highly proliferative CD4⁺ memory T cells in patients with long duration T1D awaits further investigation. Nevertheless, the ability to simultaneously identify multiple cell types and perform detailed molecular

**Figure 6. Pancreatic Tissue from HPAP020 Displays Histopathological Changes of Very Recent Onset T1D**

(A) Selected channel overlays for ROIs consisting of islets with no beta cells (upper panels) or with beta cells (lower panels). Islets with remnant beta cells exhibit increased peri- and intra-islet accumulation of immune cells. Displayed channels are as follows: left, C-PEP (green), GCG (red), and SST (blue); middle-left, CD99 (green) and CD45 (red); middle-right, CD4 (green), CD8 (red), CD20 (white), and GCG (blue); right, CD68 (green), CD45 (red), and CD56 (blue). Apart from being an NK-cell marker, CD56 also labels neurons and islets (right panels).

(legend continued on next page)

phenotyping in the same tissue section demonstrates the high content nature of the IMC platform.

Lastly, we investigated whether there was a significant difference in positivity for Ki67 in different immune cell types within the T1D donor tissues as compared to controls. Due to the small sample size, we grouped all the T1D donors together irrespective of their diabetes duration. We found that tissue-resident immune cells in T1D donor pancreata tended to have a greater frequency of proliferation than controls, although significance was only reached in the B cells and CD8⁺ T cells (Mann-Whitney test, $p \leq 0.05$) (Figure 5D).

Histopathological Observations in a Donor with Recent-Onset T1D

Finally, we focused our analyses on the pancreas of HPAP020, a 14-year-old Caucasian male donor who, with missed T1D diagnosis, passed away within days of T1D onset, as this donor held the greatest promise for detecting active insulitis (i.e., inflammation of the islets of Langerhans). In this donor, serum autoantibodies were quadruple positive for GAD65A, IA-2A, IAA, and ZnT8A (Table S4). We detected substantial heterogeneity in disease histopathology from this donor depending on anatomic location. For instance, remnant beta cells were detected only in the tail region of the pancreas (Figure 6A). Intriguingly, CD45⁺ immune cells (particularly CD8⁺ T cells, but also CD4⁺ T cells, CD20⁺ B cells, and macrophages) were present in close proximity to these beta cell-containing islets in a polarized fashion (Figure 6A, bottom panel). Peri-islet immune infiltration was also detected in the head and body of the pancreas from this donor, although the islets were more fragmented and lacking in beta cells (Figure 6A, top panel). Because of the limited number of sections surveyed, we cannot exclude the possibility that islets with residual beta cells may have also existed in the head and body regions of the pancreas. Our analyses nevertheless present snapshots of different stages of beta cell destruction within the same donor.

We categorized the islet regions based on the presence or absence of beta cells and quantified the immune cells within different distance ranges relative to islets. B cells and CD8⁺ T cells were significantly enriched in the islet proximal area (within and up to 20 μm to islets) in the regions with remnant beta cells compared with those containing no beta cells (multiple t tests, false discovery rate (FDR) < 10%) (Figure 6B). In the islet distal area (20–70 μm in distance), CD8⁺ immune cell density was significantly elevated in regions containing beta cells compared with those lacking beta cells (multiple t tests, FDR < 10%) (Figure 6C). In addition, compared with controls, remnant beta cells

in this donor displayed dramatic and significant upregulation of HLA-ABC expression among all endocrine and ductal cell types (two-way ANOVA with Tukey method, FWER < 0.05) (Figure 6D; violin with red outline). IMC data confirmed the upregulation of HLA-ABC in beta cells (Figure 6E). Hyperexpression of HLA-ABC in beta cells of patients with T1D had been postulated to be one of the mechanisms that render beta cells visible to CD8⁺ cytotoxic T cells (Bottazzo et al., 1985; Coppieters et al., 2012).

DISCUSSION

IMC is a powerful platform for highly multiplexed measurements of protein abundance and localization in the human pancreas. This technology combines single-cell spatial resolution with high sensitivity. Data generated from IMC supports detailed histological phenotyping including direct visualization and quantification of various cell types and subsets typified by the expression of protein markers. Here, we optimized a staining protocol for IMC on FFPE sections of human pancreatic tissue. We have established and validated an antibody panel, including a combination of 33 different markers and an imaging analysis pipeline, that facilitates large-scale quantitative analyses of human pancreata from control donors as well as donors with different durations of T1D. With an array of protein expression data, we were able to simultaneously identify major pancreatic and immune cell types and quantify complex cellular interactions during T1D progression. We found dramatic changes in islet architecture, endocrine cell number, and immune cell number in the T1D pancreata (Figures 2, 3, and 6). We also observed molecular changes indicating altered cell identity and dysregulated cellular protein expression in the histopathology of T1D (Figures 4, 5, and 6).

The quantification of all immune cell types present within or in direct contact with an islet suggests that the degree of immune-cell infiltration can differ considerably within and between donors. Multiple criteria have been proposed for the definition of human insulitis in the past, with a minimal cutoff of 2 (Itoh et al., 1993), 5 (Willcox et al., 2009), or 15 CD45⁺ cells (Campbell-Thompson et al., 2013) within the islet or at the exocrine-islet interface. This variable threshold is partially due to different sensitivities of the detection platforms employed by various investigators. Therefore, accurate baseline quantification of control donors is critical in order to set the appropriate threshold for islet inflammation. In addition, an absolute threshold does not take islet size into consideration and is biased toward bigger islets simply because they have a larger area. In the current study,

(B) Quantification of immune cells proximal to islets (inside islets or within a 20- μm halo extending from islets) and stratified by islets with or without beta cells. Cell numbers are normalized to 1 mm^2 regions. Each dot represents one ROI. All ROIs are from the same donor HPAP020. Islets with beta cells have significantly higher numbers of B cells and CD8⁺ T cells in their immediate vicinity than those lacking beta cells. *, FDR < 10%, calculated from t tests with multiple comparison correction.

(C) Quantification of immune cells 20–70 μm distal to islets. Cell numbers are normalized to 1 mm^2 region. Each dot represents one ROI. All ROIs are from HPAP020. Halos surrounding islets with beta cells have significantly higher numbers of CD8⁺ T cells than those lacking beta cells. *, FDR < 10%. Statistics are calculated as in (B).

(D) Violin plots demonstrate that beta cells from HPAP020 have elevated expression of HLA-ABC compared with controls. HLA-ABC expressions of individual cells from HPAP020 or control donors are used as input. two-way ANOVA with Tukey method is used for statistical testing, with FWER < 0.05. Compared with all the other cell types in HPAP020 and control donors, beta cells in HPAP020 (violin with red outline) have significantly higher levels of HLA-ABC expression.

(E) IMC data confirm the upregulation of HLA-ABC in this donor. Displayed channels are as follows: HLA-ABC (green), GCG (red), and C-PEP (blue).

we normalized the number of immune cells either to the total number of cells (immune or non-immune) within each area (Figures 3C and 3D) or the absolute area considered (Figures 6B and 6C).

Our observation of alpha cells in T1D donors expressing the canonical beta cell transcription factor NKX6.1 confirms recent findings of Brissova and colleagues using conventional immunofluorescence staining (Figures 4C and 4D) (Brissova et al., 2018). It is tempting to speculate that this observation represents partial transdifferentiation of alpha cells toward the beta cell fate in response to chronic hyperglycemia. Human alpha cells were shown to exist in a plastic epigenetic state, indicated by the presence of thousands of bivalent histone marks on genes typically expressed in beta cells (Bramswig et al., 2013). In addition, human alpha cells maintain twice the rate of proliferation than that of beta and delta cells throughout the human lifespan (Wang et al., 2016). Mouse models have provided direct evidence of the plasticity of alpha cells. For example, it was shown that alpha cells can transdifferentiate into beta cells under conditions of near-absolute beta-cell deficiency (Thorel et al., 2010). Recently, genetic lineage tracing in mice demonstrated that a small fraction of alpha cells transdifferentiate into insulin-producing beta cells throughout adulthood under normal homeostasis, supporting the notion of alpha cells as a potential “reserved pool” for generation of additional beta cells in times of need (van der Meulen et al., 2017; Ackermann et al., 2018). However, whether such transdifferentiation occurs and is ever complete in humans remains to be established.

There are several important advantages of IMC: (1) quantitative protein-level assessment can be performed efficiently for dozens of proteins in parallel and (2) cellular phenotypes are recorded *in situ* within the tissue context. As a result, spatial relationships and morphological features are preserved. Additionally, for FFPE sections, all cells are fixed to preserve their cellular state. Any stress introduced by cell isolation and subsequent alterations of cell physiology can be avoided. We anticipate the IMC technology to be readily implemented to study metabolic disorders including various forms of diabetes. Importantly, because of its capability to simultaneously measure more than 30 markers in the same tissue section, the IMC platform will be very useful in the clinical setting where tissue quantities from patient biopsies are limited. During the revision of the manuscript, two additional multiplexed image systems were reported (Goltsev et al., 2018; Gut et al., 2018). Together with IMC, these systems allow for the inclusion of a variety of markers for sophisticated pathological analyses.

Limitations of Study

There are, however, limitations of the IMC platform. IMC can have low sensitivity for some proteins since there is no option to increase “exposure time” as generally achievable with fluorescence-based imaging platforms. Because of detection limits and the limited precision of the laser spot, the X-Y resolution of IMC is set at 1 μm. The Z resolution is dependent on the thickness of tissue sections, which is typically 4–8 μm. This is enough for cell-level analysis since average epithelial cell size is approximately 10 μm. However, at this resolution, it is difficult to perform subcellular analysis. In addition, the IMC acquisition process is time consuming, as it takes about 2 h to ablate a 1,000 μm ×

1,000 μm ROI. The slow rate of image acquisition not only impairs system throughput but also introduces the potential for batch effects resulting from instrument drifts. In the current work, we made an effort to reduce batch effects between different tissue sections by performing staining using the same master mix with randomized samples. IMC is also disruptive to tissue, and consequently, orthogonal experimental procedures cannot be performed on the same tissue section.

Another limitation of IMC technology and by extension, of all image-based technology, is limited tissue sampling. For the current study, the IMC data for the 18 donors came from acquisition of multiple ROIs from one tissue section from each anatomical region within the pancreas. This can potentially introduce analysis bias and may contribute to the minor differences observed between the quantification of IMC and CyTOF (Figures S3C and S3D), wherein the latter data came from islets isolated from the entire pancreas. Yet, this limitation is otherwise compensated in IMC by added spatial information and combinatorial protein measurement with cellular resolution. Moreover, as discussed above, analyses on fixed tissue *in situ* preserve the native cellular states and avoid any enrichment or depletion that may be introduced by an islet isolation procedure. This current work, together with the co-submitted work by Damond and colleagues (Damond et al., 2019), has established the IMC technology to perform highly multiplexed imaging analyses of the human pancreas, and it will be possible to apply the platform to much larger sample sizes in the future. We hope that this technology will become an important tool in the arsenal for diabetes researchers to obtain the maximum amount of information from rare tissue samples.

STAR★METHODS

Detailed methods are provided in the online version of this paper and include the following:

- KEY RESOURCES TABLE
- CONTACT FOR REAGENT AND RESOURCE SHARING
- EXPERIMENTAL MODEL AND SUBJECT DETAILS
- METHOD DETAILS
 - Antibody Validation
 - Antibody Labeling and Image Acquisition
 - Signal Compensation
 - Hot Pixel Removal
 - Image Segmentation
 - Cell Type Calling
- QUANTIFICATION AND STATISTICAL ANALYSIS
- DATA AND SOFTWARE AVAILABILITY

SUPPLEMENTAL INFORMATION

Supplemental Information includes six figures and six tables and can be found with this article online at <https://doi.org/10.1016/j.cmet.2019.01.003>.

ACKNOWLEDGMENTS

We thank the families of the organ donors without whom this study would not have been possible. We thank Dr. Andrew Raim for statistical consultation. This research was performed using resources and/or funding provided by the NIDDK-supported Human Islet Research Network (HIRN, RRID:SCR_014393;

<https://hirnetwork.org>) grants UC4 DK112217 to A.N., UC4 DK112232 to A.C.P., UC4 DK108132 to M.A.A., and UC4 DK104119 to K.H.K.; the University of Pennsylvania Diabetes Research Center (P30 DK19525); the Vanderbilt Diabetes Research and Training Center (P30 DK20593); and the Department of Veterans Affairs. This research was performed with the support of the Network for Pancreatic Organ Donors with Diabetes (nPOD), a collaborative type 1 diabetes research project sponsored by JDRF. Organ procurement organizations partnering with nPOD to provide research resources are listed at <http://www.jdrfnpod.org//for-partners/npod-partners/>.

AUTHOR CONTRIBUTIONS

Y.J.W. researched the data and wrote the manuscript. D.T. acquired raw imaging data. J.S. performed imaging processing and data analyses. L.G. carried out signal compensation. C.L. and the HPAP Consortium isolated human pancreata. M.A.A. and A.C.P. contributed to discussion and reviewed and edited the manuscript. K.H.K., M.D.F., A.N., and K.-M.C. conceived of the study and wrote the manuscript.

DECLARATION OF INTERESTS

The authors declare no competing interests.

Received: April 10, 2018

Revised: September 15, 2018

Accepted: January 7, 2019

Published: January 31, 2019

WEB RESOURCES

Human Pancreas Analysis Program (HPAP), <https://hpap.pmacs.upenn.edu/>.

REFERENCES

- Ackermann, A.M., Moss, N.G., and Kaestner, K.H. (2018). GABA and artesunate do not induce pancreatic alpha- to beta-cell transdifferentiation in vivo. *Cell Metab.* 28, 787–792.
- American Diabetes Association (2009). Diagnosis and classification of diabetes mellitus. *Diabetes Care* 33, S62–S69.
- Angelo, M., Bendall, S.C., Finck, R., Hale, M.B., Hitzman, C., Borowsky, A.D., Levenson, R.M., Lowe, J.B., Liu, S.D., Zhao, S., et al. (2014). Multiplexed ion beam imaging of human breast tumors. *Nat. Med.* 20, 436–442.
- Asadi, A., Bruin, J.E., and Kieffer, T.J. (2015). Characterization of antibodies to products of proinsulin processing using immunofluorescence staining of pancreas in multiple species. *J. Histochem. Cytochem.* 63, 646–662.
- Atkinson, M.A. (2012). The pathogenesis and natural history of type 1 diabetes. *Cold Spring Harb. Perspect. Med.* 2, a007641.
- Atkinson, M.A. (2014). Pancreatic biopsies in type 1 diabetes: revisiting the myth of Pandora's box. *Diabetologia* 57, 656–659.
- Atkinson, M.A., and Eisenbarth, G.S. (2001). Type 1 diabetes: new perspectives on disease pathogenesis and treatment. *Lancet* 358, 221–229.
- Atkinson, M.A., Eisenbarth, G.S., and Michels, A.W. (2014). Type 1 diabetes. *Lancet* 383, 69–82.
- Bogdani, M., Korpos, E., Simeonovic, C.J., Parish, C.R., Sorokin, L., and Wight, T.N. (2014). Extracellular matrix components in the pathogenesis of type 1 diabetes. *Curr. Diab. Rep.* 14, 552.
- Bonner-Weir, S., and Orci, L. (1982). New perspectives on the microvasculature of the islets of Langerhans in the rat. *Diabetes* 31, 883–889.
- Bottazzo, G.F., Dean, B.M., McNally, J.M., MacKay, E.H., Swift, P.G., and Gamble, D.R. (1985). In situ characterization of autoimmune phenomena and expression of HLA molecules in the pancreas in diabetic insulitis. *N. Engl. J. Med.* 313, 353–360.
- Bramswig, N.C., Everett, L.J., Schug, J., Dorrell, C., Liu, C., Luo, Y., Streeter, P.R., Naji, A., Grompe, M., and Kaestner, K.H. (2013). Epigenomic plasticity enables human pancreatic α to β cell reprogramming. *J. Clin. Invest.* 123, 1275–1284.
- Brissova, M., Haliyur, R., Saunders, D., Shrestha, S., Dai, C., Blodgett, D.M., Bottino, R., Campbell-Thompson, M., Aramandla, R., Poffenberger, G., et al. (2018). α cell function and gene expression are compromised in type 1 diabetes. *Cell Rep.* 22, 2667–2676.
- Campbell-Thompson, M., Wasserfall, C., Kaddis, J., Albanese-O'Neill, A., Staeva, T., Nierras, C., Moraski, J., Rowe, P., Gianani, R., Eisenbarth, G., et al. (2012). Network for Pancreatic Organ Donors with Diabetes (nPOD): developing a tissue biobank for type 1 diabetes. *Diabetes Metab. Res. Rev.* 28, 608–617.
- Campbell-Thompson, M.L., Atkinson, M.A., Butler, A.E., Chapman, N.M., Frisk, G., Gianani, R., Giepmans, B.N., von Herrath, M.G., Hyöty, H., Kay, T.W., et al. (2013). The diagnosis of insulitis in human type 1 diabetes. *Diabetologia* 56, 2541–2543.
- Carpenter, A.E., Jones, T.R., Lamprecht, M.R., Clarke, C., Kang, I.H., Friman, O., Guertin, D.A., Chang, J.H., Lindquist, R.A., Moffat, J., et al. (2006). CellProfiler: image analysis software for identifying and quantifying cell phenotypes. *Genome Biol.* 7, R100.
- Chang, Q., Ornatsky, O.I., Siddiqui, I., Loboda, A., Baranov, V.I., and Hedley, D.W. (2017). Imaging mass cytometry. *Cytometry A* 91, 160–169.
- Coppelters, K.T., Dotta, F., Amirian, N., Campbell, P.D., Kay, T.W.H., Atkinson, M.A., Roep, B.O., and von Herrath, M.G. (2012). Demonstration of islet-autoreactive CD8 T cells in insulitic lesions from recent onset and long-term type 1 diabetes patients. *J. Exp. Med.* 209, 51–60.
- Diamond, N., Engler, S., Schapiro, D., Zanotelli, V.R.T., Schapiro, D., Wasserfall, C.H., Kusmartseva, I., Nick, H.S., Thorel, F., Herrera, P.L., et al. (2019). A map of human type 1 diabetes progression by imaging mass cytometry. *Cell Metab.* 29. this issue, Published online January 31, 2019. <https://doi.org/10.1016/j.cmet.2018.11.014>.
- Eisenbarth, G.S. (1986). Type I diabetes mellitus. A chronic autoimmune disease. *N. Engl. J. Med.* 314, 1360–1368.
- Gaujoux, R., and Seoighe, C. (2010). A flexible R package for nonnegative matrix factorization. *BMC Bioinformatics* 11, 367.
- Gerich, J.E., Langlois, M., Noacco, C., Karam, J.H., and Forsham, P.H. (1973). Lack of glucagon response to hypoglycemia in diabetes: evidence for an intrinsic pancreatic alpha cell defect. *Science* 182, 171–173.
- Giesen, C., Wang, H.A.O., Schapiro, D., Zivanovic, N., Jacobs, A., Hattendorf, B., Schüffler, P.J., Grolimund, D., Buhmann, J.M., Brandt, S., et al. (2014). Highly multiplexed imaging of tumor tissues with subcellular resolution by mass cytometry. *Nat. Methods* 11, 417–422.
- Goltsev, Y., Samusik, N., Kennedy-Darling, J., Bhate, S., Hale, M., Vazquez, G., Black, S., and Nolan, G.P. (2018). Deep profiling of mouse splenic architecture with Codex multiplexed imaging. *Cell* 174, 968–981.
- Gu, G., Dubauskaite, J., and Melton, D.A. (2002). Direct evidence for the pancreatic lineage: NGN3+ cells are islet progenitors and are distinct from duct progenitors. *Development* 129, 2447–2457.
- Gut, G., Herrmann, M.D., and Pelkmans, L. (2018). Multiplexed protein maps link subcellular organization to cellular states. *Science* 361.
- Itoh, N., Hanafusa, T., Miyazaki, A., Miyagawa, J., Yamagata, K., Yamamoto, K., Waguri, M., Imagawa, A., Tamura, S., and Inada, M. (1993). Mononuclear cell infiltration and its relation to the expression of major histocompatibility complex antigens and adhesion molecules in pancreas biopsy specimens from newly diagnosed insulin-dependent diabetes mellitus patients. *J. Clin. Invest.* 92, 2313–2322.
- Korpos, É., Kadri, N., Kappelhoff, R., Wegner, J., Overall, C.M., Weber, E., Holmberg, D., Cardell, S., and Sorokin, L. (2013). The peri-islet basement membrane, a barrier to infiltrating leukocytes in type 1 diabetes in mouse and human. *Diabetes* 62, 531–542.
- Kuznetsova, A., Brockhoff, P.B., and Christensen, R.H.B. (2017). ImeTest package: tests in linear mixed effects models. *J. Stat. Soft.* 82.
- Lifson, N., Kramlinger, K.G., Mayrand, R.R., and Lender, E.J. (1980). Blood flow to the rabbit pancreas with special reference to the islets of Langerhans. *Gastroenterology* 79, 466–473.
- Malaisse-Lagae, F., Stefan, Y., Cox, J., Perrelet, A., and Orci, L. (1979). Identification of a lobe in the adult human pancreas rich in pancreatic polypeptide. *Diabetologia* 17, 361–365.

- van der Meulen, T., Mawla, A.M., DiGruccio, M.R., Adams, M.W., Nies, V., Dölleman, S., Liu, S., Ackermann, A.M., Cáceres, E., Hunter, A.E., et al. (2017). Virgin beta cells persist throughout life at a neogenic niche within pancreatic islets. *Cell Metab.* 25, 911–926.
- Mueller, P.R., Miketic, L.M., Simeone, J.F., Silverman, S.G., Saini, S., Wittenberg, J., Hahn, P.F., Steiner, E., and Forman, B.H. (1988). Severe acute pancreatitis after percutaneous biopsy of the pancreas. *AJR Am. J. Roentgenol.* 151, 493–494.
- Phillips, J.M., Parish, N.M., Bland, C., Sawyer, Y., De La Peña, H., and Cooke, A. (2009). Type 1 diabetes development requires both CD4 and CD8 T cells and can be reversed by non-depleting antibodies targeting both T cell populations. *Rev. Diabet. Stud.* 6, 97–103.
- Pihoker, C., Gilliam, L.K., Hampe, C.S., and Lernmark, A. (2005). Autoantibodies in diabetes. *Diabetes* 54, S52–S61.
- Poudel, A., Savari, O., Striegel, D.A., Periwal, V., Taxy, J., Millis, J.M., Witkowski, P., Atkinson, M.A., and Hara, M. (2015). Beta-cell destruction and preservation in childhood and adult onset type 1 diabetes. *Endocrine* 49, 693–702.
- Schaffter, A.E., Taylor, B.L., Benthuyzen, J.R., Liu, J., Thorel, F., Yuan, W., Jiao, Y., Kaestner, K.H., Herrera, P.L., Magnuson, M.A., et al. (2013). Nkx6.1 Controls a gene regulatory network required for establishing and maintaining pancreatic Beta cell identity. *PLoS Genet.* 9, e1003274.
- Schapiro, D., Jackson, H.W., Raghuraman, S., Fischer, J.R., Zanotelli, V.R.T., Schulz, D., Giesen, C., Catena, R., Varga, Z., and Bodenmiller, B. (2017). histoCAT: analysis of cell phenotypes and interactions in multiplex image cytometry data. *Nat. Methods* 14, 873–876.
- Scrucca, L., Fop, M., Murphy, T.B., and Raftery, A.E. (2016). Mclust 5: clustering, classification and density estimation using gaussian finite mixture models. *R J* 8, 289–317.
- Spijker, H.S., Song, H., Ellenbroek, J.H., Roefs, M.M., Engelse, M.A., Bos, E., Koster, A.J., Rabelink, T.J., Hansen, B.C., Clark, A., et al. (2015). Loss of β -cell identity occurs in type 2 diabetes and is associated with islet amyloid deposits. *Diabetes* 64, 2928–2938.
- Stefan, Y., Grasso, S., Perrelet, A., and Orci, L. (1982). The pancreatic polypeptide-rich lobe of the human pancreas: definitive identification of its derivation from the ventral pancreatic primordium. *Diabetologia* 23, 141–142.
- Team, R.C., et al. (2013). R: A Language and Environment for Statistical Computing (R,Foundation for Statistical Computing). <https://www.r-project.org/>.
- Thorel, F., Népote, V., Avril, I., Kohno, K., Desgraz, R., Chera, S., and Herrera, P.L. (2010). Conversion of adult pancreatic α -cells to β -cells after extreme β -cell loss. *Nature* 464, 1149–1154.
- Wang, G., Rajpurohit, S.K., Delaspere, F., Walker, S.L., White, D.T., Cesarine, A., Kuruvilla, R., Li, R.J., Shim, J.S., Liu, J.O., et al. (2015). First quantitative high-throughput screen in zebrafish identifies novel pathways for increasing pancreatic β -cell mass. *Elife* 4.
- Wang, X., Misawa, R., Zielinski, M.C., Cowen, P., Jo, J., Periwal, V., Ricordi, C., Khan, A., Szust, J., Shen, J., et al. (2013). Regional differences in islet distribution in the human pancreas—preferential beta-cell loss in the head region in patients with type 2 diabetes. *PLoS One* 8, e67454.
- Wang, Y.J., Golson, M.L., Schug, J., Traum, D., Liu, C., Vivek, K., Dorrell, C., Naji, A., Powers, A.C., Chang, K.M., et al. (2016). Single-cell mass cytometry analysis of the human endocrine pancreas. *Cell Metab.* 24, 616–626.
- Willcox, A., Richardson, S.J., Bone, A.J., Foulis, A.K., and Morgan, N.G. (2009). Analysis of islet inflammation in human type 1 diabetes. *Clin. Exp. Immunol.* 155, 173–181.
- Xin, Y., Kim, J., Okamoto, H., Ni, M., Wei, Y., Adler, C., Murphy, A.J., Yancopoulos, G.D., Lin, C., and Gromada, J. (2016). RNA sequencing of single human islet cells reveals type 2 diabetes genes. *Cell Metab.* 24, 608–615.

STAR★METHODS

KEY RESOURCES TABLE

REAGENT or RESOURCE	SOURCE	IDENTIFIER
Deposited Data		
Additional raw data	This paper/Mendeley Data	http://dx.doi.org/10.17632/9b262xmtrm9.1 and http://dx.doi.org/10.17632/xbxnfg2zfs.1
Antibodies		
HLA-ABC (Clone EMR8-5)	BD Biosciences	Cat#565292
142nd-CD57 (Clone HCD57)	Fluidigm	Cat#3142007B
CD31 (Clone C31.3+C31.7+C31.10)	LifeSpan BioSciences	Cat#LS-C390863-100
144Nd-CD14 (Clone EPR3653)	Fluidigm	Cat#3144025D
PROINSULIN/C-PEPTIDE (Clone 3A1)	Thermo	Cat#MA1-22710; RRID: AB_558517
146Nd-NESTIN (Clone 196908)	Fluidigm	Cat#3146015B
GLUCAGON (Clone C-11)	Santa Cruz	Cat#sc-514592; RRID: AB_2629431
148Nd-Pan-Keratin (Clone C11)	Fluidigm	Cat#3148020D
149Sm-CD11b (Clone EPR1344)	Fluidigm	Cat#3149028D
150Nd-CD44 (Clone IM7)	Fluidigm	Cat#3150018B
PDX1	R&D systems	Cat#AF2419; RRID: AB_355257
152Sm-CD45 (Clone 2B11)	Fluidigm	Cat#3152016D
152Sm-CD45 (Clone D9M8I)	Fluidigm	Cat#3152018D
CD56	Proteintech	Cat#14255-1-AP; RRID: AB_2149421
154Sm-β-AXTIN (Clone 2F1-1)	Fluidigm	Cat#3154021D
155Gd-FOXP3 (Clone 236A/E7)	Fluidigm	Cat#3155016D
156Gd-CD4 (Clone EPR6855)	Fluidigm	Cat#3156033D
NKX6.1	Sigma	Cat#HPA036774; RRID: AB_10673664
159Tb-CD68 (Clone KP1)	Fluidigm	Cat#3159035D
SOMATOSTATIN	Santa Cruz	Cat#sc-13099; RRID: AB_2195930
161Dy-CD20 (Clone H1)	Fluidigm	Cat#3161029D
162Dy-CD8 (Clone C8/144B)	Fluidigm	Cat#3162034D
CD99	R&D systems	Cat#AF3968; RRID: AB_2076301
CA2	Rockland	Cat#200-401-136S; RRID: AB_2612117
166Er-NF-κB (Clone K10895.12.50)	Fluidigm	Cat#3166006A
167Er-GRANZYME B (Clone EPR20129-217)	Fluidigm	Cat#3167021D
168Er-Ki67 (Clone B56)	Fluidigm	Cat#3168022D
169Tm-Collagen Type 1	Fluidigm	Cat#3169023D
170Er-CD3	Fluidigm	Cat#3170019D
172Yb-pS6 (Clone N7-548)	Fluidigm	Cat#3172008A
173Yb-CD45RO (Clone UCHL1)	Fluidigm	Cat#3173016D
HLA-DR (Clone TAL 1B5)	Abcam	Cat#ab20181; RRID: AB_445401
PANCREATIC POLYPEPTIDE	Abcam	Cat#ab77192; RRID: AB_1524152
GHRELIN	Santa Cruz	Cat#sc-10368; RRID: AB_2232479
Software and Algorithms		
CellProfiler Version 3.0.0	Carpenter et al., 2006	http://cellprofiler.org/
Cytobank		https://www.cytobank.org/
R Version 3.4.1 (2017-06-30)	R Core Team, 2013	http://www.R-project.org/
ImerTest Version 2.0-36	Kuznetsova et al., 2017	https://cran.r-project.org/web/packages/ImerTest/index.html
tiff Version 0.1-5	Urbanek, 2013	https://CRAN.R-project.org/package=tiff

(Continued on next page)

Continued

REAGENT or RESOURCE	SOURCE	IDENTIFIER
Igraph Version 1.2.1	Csardi and Nepusz, 2006	http://igraph.org
GetoptLong Version 0.1.6	Gu, 2017	https://CRAN.R-project.org/package=GetoptLong
Magrittr Version 1.5	Bache and Wickham, 2014	https://CRAN.R-project.org/package=magrittr
dplyr Version 0.7.4	Wickham et al., 2017	https://CRAN.R-project.org/package=dplyr
Raster Version 2.6-7	Hijmans, 2017	https://CRAN.R-project.org/package=raster
mclust Version 5.4	Scrucca et al., 2016	https://cran.r-project.org/web/packages/mclust/index.html
NMF Version 0.21.0	Gaujoux and Seoighe, 2010	https://cran.r-project.org/web/packages/NMF/index.html
histoCAT Version 1.73	Shapiro et al., 2017	https://github.com/BodenmillerGroup/histoCAT
Other		
Image data	This paper	N/A

CONTACT FOR REAGENT AND RESOURCE SHARING

Further information and requests for resources and reagents should be directed to and will be fulfilled by the Lead Contact, Klaus Kaestner (kaestner@pennmedicine.upenn.edu).

EXPERIMENTAL MODEL AND SUBJECT DETAILS

Formalin-fixed paraffin-embedded (FFPE) pancreatic tissue sections from human donors with or without T1D were procured from the nPOD biorepository (www.jdrfnpod.org) and through the HPAP consortium (<https://hpap.pmacs.upenn.edu/>) under Human Islet Research Network (<https://hirnetwork.org/>) with approval from the University of Florida Institutional Review Board (IRB# 201600029) and the United Network for Organ Sharing (UNOS). Prior to organ retrieval, informed consent was provided by each donor's legal representative. Medical chart review and C-peptide measurement was performed to confirm or determine T1D diagnosis according to American Diabetes Association guidelines ([American Diabetes Association, 2009](#)), and organ recovery and processing occurred as previously described ([Campbell-Thompson et al., 2012](#)). Donor information is provided in [Table S4](#).

METHOD DETAILS**Antibody Validation**

20 of the 33 antibodies used in the current panel were directly purchased from Fluidigm^R (<https://www.fluidigm.com>). For the remaining 13 antibodies, carrier-free antibodies were purchased from different vendors and tested by immunofluorescent staining on FFPE sections. Based on anticipated epitope abundance, either pancreas or spleen sections were used for antibody testing. The staining results of antibodies were assessed by board-certified pathologists. Antibodies producing the expected results were conjugated with lanthanide metals using the Maxpar X8 metal conjugation kit following manufacturer's protocol (Fluidigm 201300). Post-conjugation, antibody specificities were again tested using immunofluorescent staining, followed by titration in the IMC platform. The antibody characterization procedure and results are shown in [Figures S1A](#) and [S1B](#) and [Table S1](#). More details on antibody quality assessment can be found in [Tables S2](#) and [S3](#).

Antibody Labeling and Image Acquisition

Four to eight μm FFPE sections were stained with an antibody cocktail ([Table S1](#)) containing all antibodies. Briefly, tissue sections were de-paraffinized with xylene and carried through sequential rehydration from 100% Ethanol to 70% Ethanol before being transferred to PBS. Heat-induced antigen retrieval was performed in a decloaking chamber (Biocare Medical) at 95°C for 30 min in Tris/EDTA buffer (10mM Tris, 1mM EDTA, pH9.2). Slides were cooled to room temperature (RT) and were subsequently blocked with PBS+3%BSA for 1 h at RT. Meanwhile, the antibody cocktail was prepared in PBS+1%BSA buffer, with the appropriate dilution for each of the antibodies ([Table S1](#)). Each slide was incubated with 100 μl of the antibody cocktail overnight at 4°C. The next day, slides were washed 3 times with PBS and labeled with 1:400 dilution of Intercalator-Ir (Fluidigm 201192B) in PBS for 30 min at RT. Slides were briefly washed with H₂O three times and air dried for at least 30 min before IMC acquisition. The IMC was purchased from Fluidigm (Fluidigm, Hyperion Imaging System). All IMC operation was performed following Fluidigm's operation

procedure. Briefly, following daily tuning of IMC, image acquisition was carried out following manufacturer's instruction at a laser frequency of 200 Hz. $1,000 \mu\text{m} \times 1,000 \mu\text{m}$ regions around islets were selected based on bright field images.

Signal Compensation

Despite of the significantly lower channel crossover in IMC compared to immunofluorescent signals, small but noticeable bleed-through still exists. For a given channel M, the crosstalk signals may be contributed by isotopes with mass differences between $\pm(1-3)$ M, by impurities of isotopes of the same element, or by oxidation from the M-16 channel. To systematically compensate for signal crossover, we plotted pairwise pixel intensity between channel M and all of the potential spillover-contributing channels in the \log_2 scale. Crossover was evidenced by "tail" like linear structures in which pixels had high values in both channels. Signals were considered a crosstalk when there were less than 10 pixels in between the off-axial pixels and the axis of potential spillover-contributing channel within the ± 1 intensity region. Next, we combined the sets of pixels from multiple bleeding channels and compensated them by resampling their intensity values in M and maintaining their original values from bleeding contributing channels. Examples of signals before and after compensation are shown in [Figure S2A](#).

Hot Pixel Removal

Prior to quantification of cellular regions, 'hot pixels' and streaks were removed with a median filter using a 5×5 pixel² window that excludes the middle row (based on the observation that background streaks often show as horizontal lines). The center pixel was assigned the median value in the window when the center pixel is in the top 2% of pixel values and was at least 4x above the median value of all pixels in the window. Thus, only outlier pixel values were adjusted and only when they were also distinct from their neighboring pixels in a vertical direction. The vertical aspect ensures that adjacent pixels in a streak do not artificially increase the median value, while still keeping the neighborhood small to avoid over-smoothing. Protein expression values for each cell were set to the mean of pixel values in each cell mask region.

Image Segmentation

All segmentation was implemented in CellProfiler (3.0.0) ([Carpenter et al., 2006](#)). For islet segmentation, all hormone markers (i.e., C-PEP, GCG, SST, GHRL and PP) were thresholded and their binarized values were added under image math module. Gaussian Filter was then applied to the binarized image to fill in holes. The boundaries of combined hormone regions were then defined by a global threshold strategy with the minimum cross entropy method. Islet area and other measurement of islets were directly conducted using the MeasureObjectSizeShape module. The area of the exocrine tissue was identified by thresholded CD99-positive area masked against islets. The peri-islet regions used for collagen measurement were defined using ExpandOrShrinkObjects and MaskObjects module, by selecting the 10-pixel wide outer rings of the islet objects. Similarly, the islets+20 μm and 20–70 μm regions were constructed by expanding the islet masks by corresponding pixel values. The resulting masks were overlaid onto raw tiff images for visualization with histoCAT Version 1.73 ([Schapiro et al., 2017](#)).

For cell segmentation of nonimmune cells, we employed DNA-Iridium and CD99 staining as nuclear and cell membrane markers to define primary and secondary objects. Since the CD99 signal was stronger in islets compared with the exocrine tissue, histogram equalization was performed in imageJ with Enhance Local Contrast (CLAHE) function (blocksize=39, histogram bins=256, maximum slope=40, mask=None). Two independent masks for each image set were generated by two different investigators. Intensities for different antibody channels within each cell were represented by mean intensity. For immune cell segmentation, DNA-Iridium was used to define the primary nucleus object. CD45 and CD68 staining were thresholded and then combined to serve as the membrane marker for secondary object identification.

Cell Type Calling

For systematic identification of cell types in all donors, we integrated several methods to assess levels of significant expression in order to ascertain positive versus negative cutoffs in each marker channel. Raw pixel intensity values were first adjusted for crosstalk, followed by hot pixel removal (see corresponding method sessions). Mean pixel intensities for each antibody channel in each cell mask were used as input for cell-type calling. The mclust function ([Scrucca et al., 2016](#)) was applied to deconvolute the distribution of the $\log_2(\log_2(\text{mean intensity} + 1))$ per channel per ROI into a model with finite normal mixtures ([Figures S2C and S2D](#)). Next, the negative population was identified either as the mode of the distribution for less abundant markers, or manually curated for more abundant markers. Thereafter, the $\log_2(\log_2(\text{mean intensity} + 1))$ distribution was shifted so that the mean expression of the negative populations was aligned at 0 for all markers. Subsequently, a sliding window was employed to identify the positive threshold for each channel for each ROI and to ensure that the positive population (defined by the cells with signal intensity above the sliding window) overlapped with the original positive staining pattern ([Figures S2C and S2D](#)). Cell types were assigned based on thresholded channels through a combination of Boolean rules as detailed in [Table S5](#). All algorithms were implemented in R with corresponding packages shown in the [Key Resources Table](#).

QUANTIFICATION AND STATISTICAL ANALYSIS

For data associated with [Figures 2B–2G](#), [3A–3D](#), and [4B](#), statistical analyses were performed with linear mixed-effects model with individual donor effect adjusted as random effect. Significant level was set at $p \leq 0.05$ and the analyses were implemented by the

lmerTest package (Version 2.0-36) (Kuznetsova et al., 2017) in R Version 3.4.1 (Team et al., 2013). For Figures 2B–2G, 3C, and 3D, data associated with individual islets were used as input. For Figures 3A and 3B, the numbers of endocrine cells associated with individual ROI were used as input. For Figure 4B, data associated with individual beta cell were used as input. For Figure 5D, Mann-Whitney test with $p \leq 0.05$ was used for statistical testing. Ki67 percentages of control and T1D donors were used as input. For Figures 6B and 6C, multiple t tests with two-stage Benjamini, Krieger and Yekutieli FDR approach were applied for significance testing, with a FDR cutoff of 10%. The test was implemented by GraphPad Prism Version 7.0a. Raw data associated with each ROI within the same donor (HPAP020) were used as input. For Figure 6D, two-way ANOVA with Tukey post hoc multiple comparisons was performed, implemented by aov and Tukey HSD functions in R, with a FWER < 0.05 as significant cutoff. HLA-ABC expressions for each individual cell in either HPAP020 or control donors were used as input. The heatmaps in Figures 4A, 5A, and S3A were generated with a heat map function in the NMF package (Version 0.21.0) (Gaujoux and Seoighe, 2010) in R. Linear regressions in Figures S2E–S2H, S4, and S5 were performed with the lm function in R. Details of statistical analyses were also given in the main text and figure legends for the corresponding figures.

DATA AND SOFTWARE AVAILABILITY

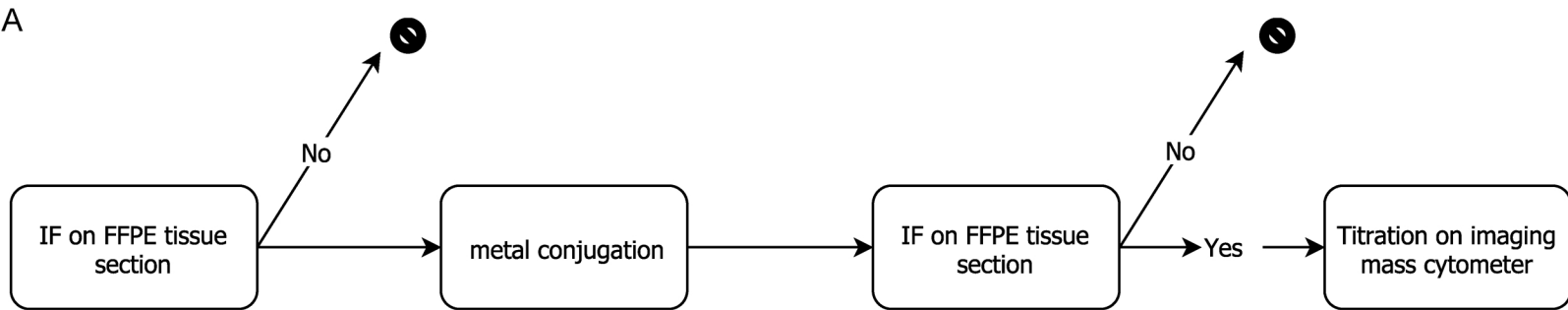
Raw image data will be available to download from the HPAP consortium website: <https://hpap.pmacs.upenn.edu/>. Additional raw data are available for download from Mendeley Data: <http://dx.doi.org/10.17632/9b262xmtm9.1> and <http://dx.doi.org/10.17632/xbxnfg2zfs.1>.

Supplemental Information

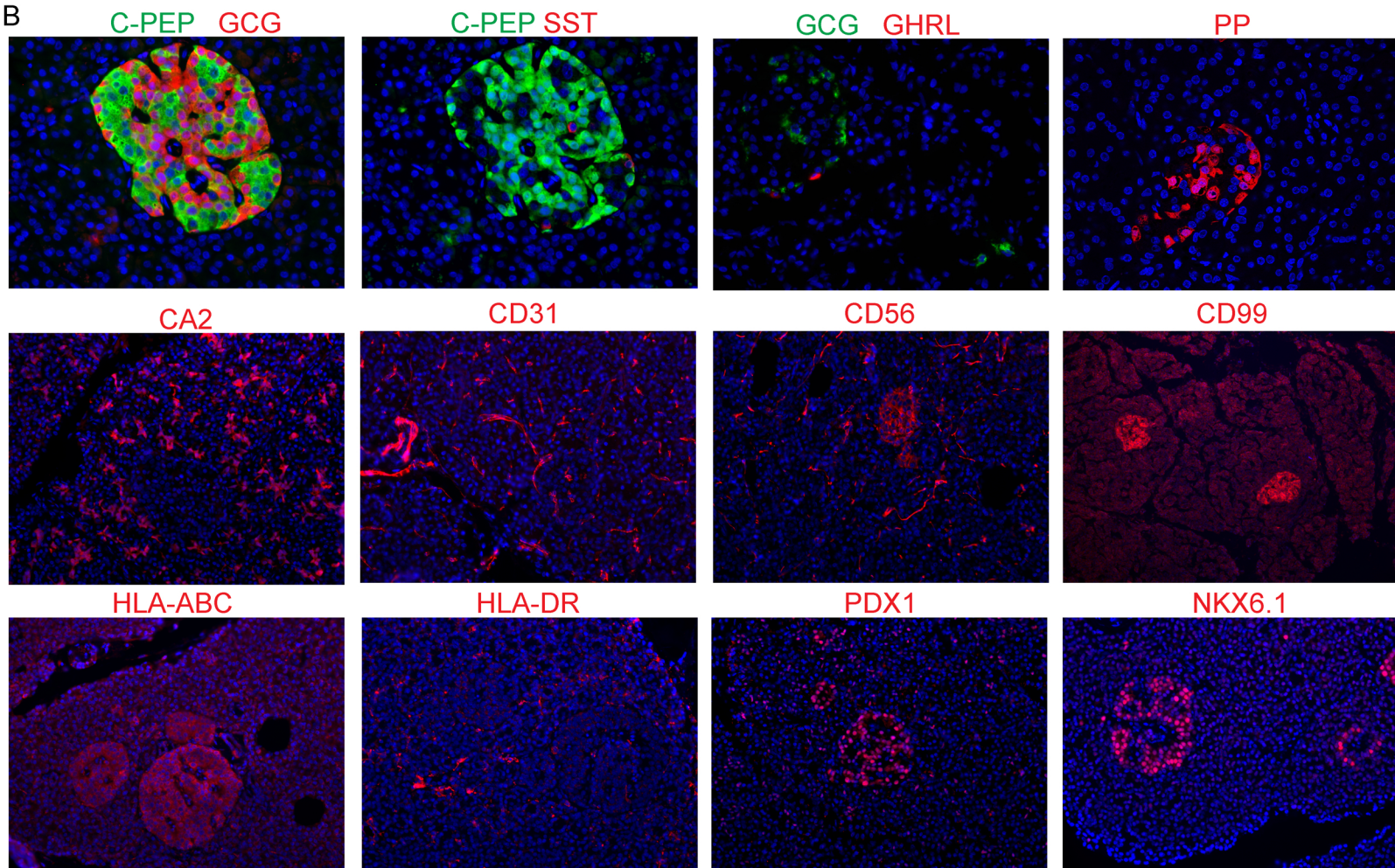
**Multiplexed *In Situ* Imaging Mass Cytometry
Analysis of the Human Endocrine Pancreas
and Immune System in Type 1 Diabetes**

Yue J. Wang, Daniel Traum, Jonathan Schug, Long Gao, Chengyang Liu, HPAP Consortium, Mark A. Atkinson, Alvin C. Powers, Michael D. Feldman, Ali Naji, Kyong-Mi Chang, and Klaus H. Kaestner

A



B



Supplementary Figure 1. Antibody validation. Related to Figure 1.

(A) Antibody validation pipeline.

(B) Immunofluorescent staining on FFPE sections is performed for the 13 newly developed heavy metal conjugated antibodies. Expected staining patterns are confirmed by pathologists. In all panels, the blue signal corresponds to DAPI staining for DNA. Displayed channels for each panel from top to bottom, left to right are: C-PEP (green)/GCG (red)/SST(white), GCG (green)/GHRL (red), GCG (green)/PP (red), CA2 (red), CD31 (red), CD56 (red), CD99 (red), HLA-ABC (red), HLA-DR (red), PDX1 (red), NKX6.1 (red), and NF-κB (red). Iridium-DNA staining is shown in blue in all panels.

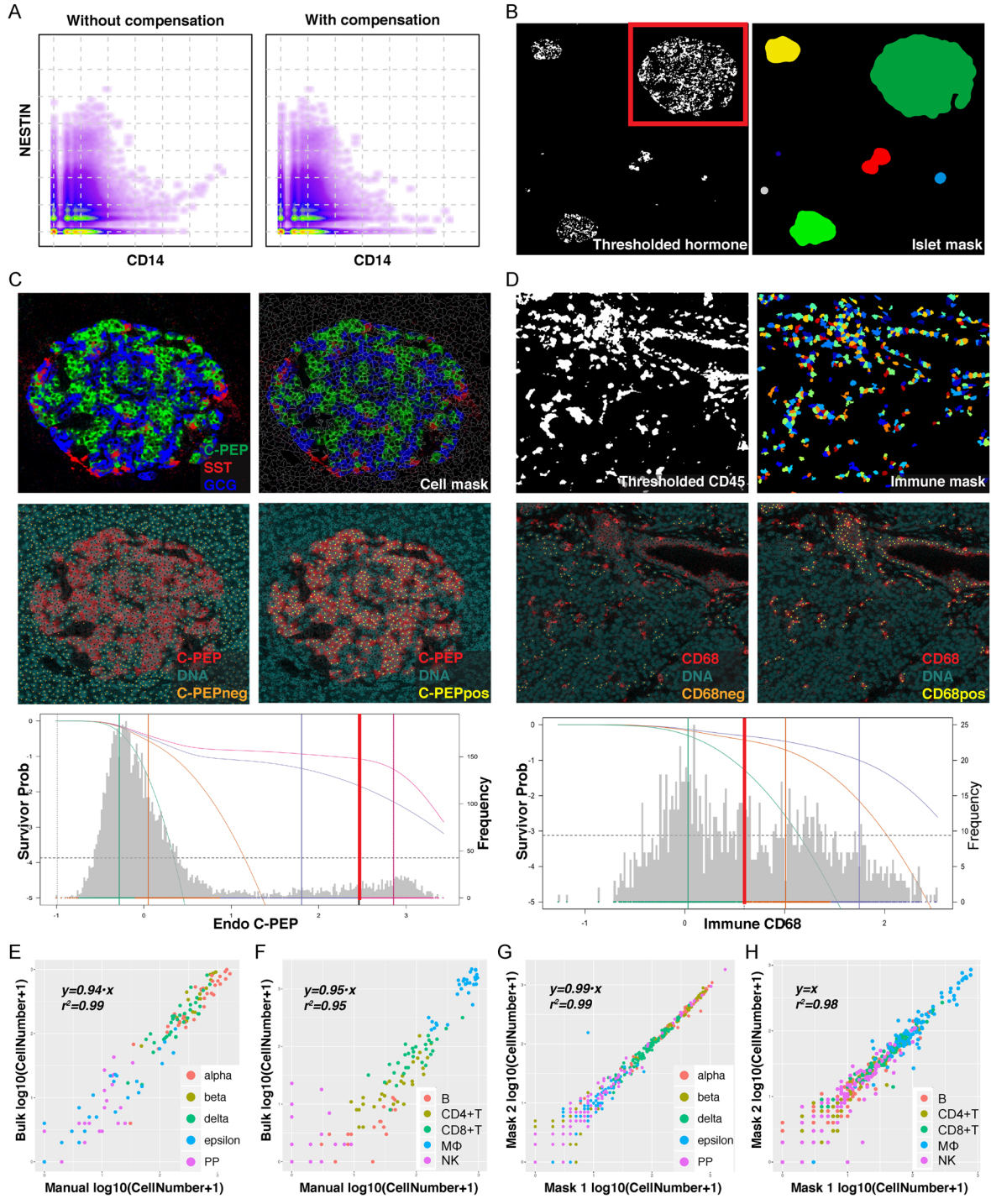
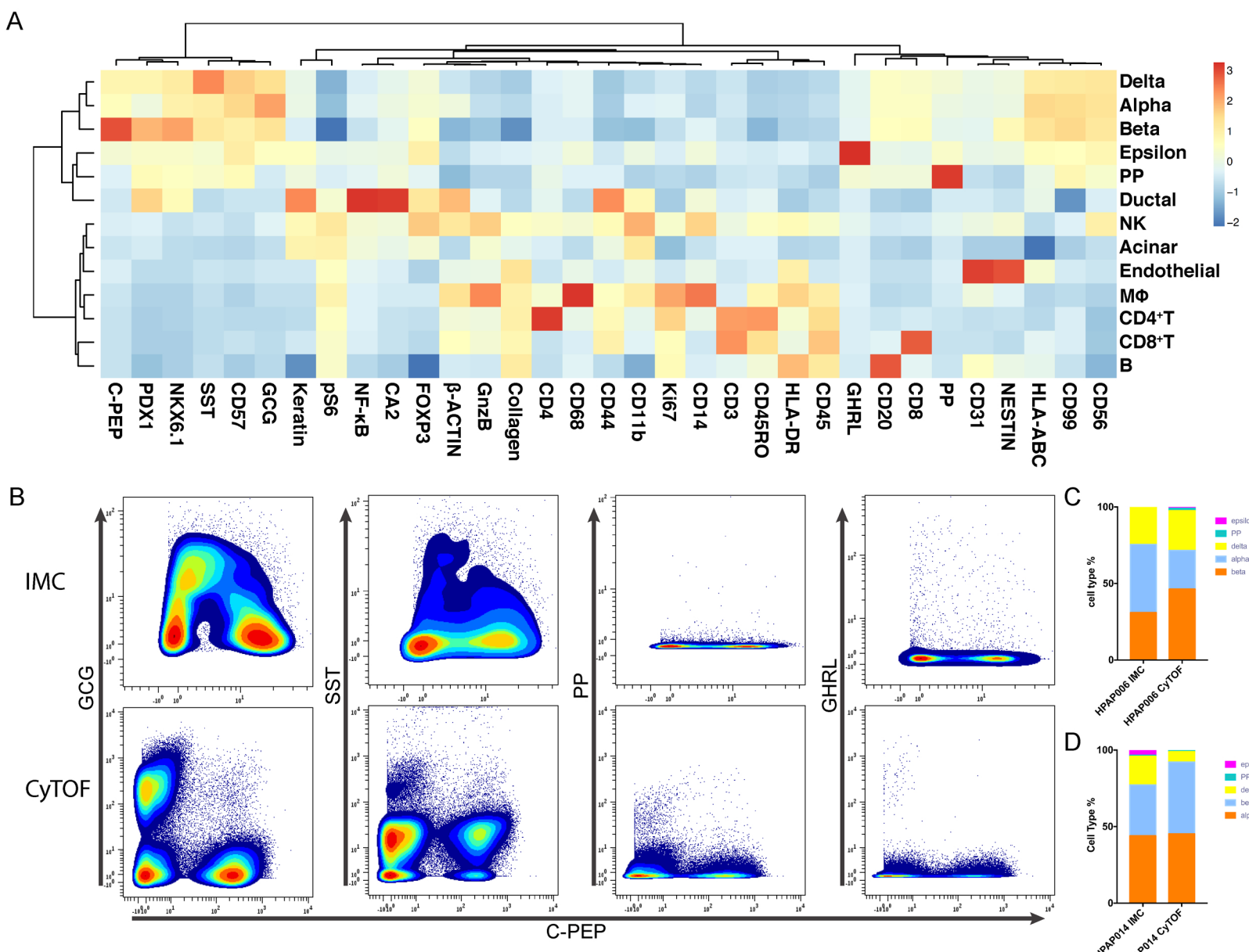


FIGURE S2

Supplementary Figure 2. Image data processing and cell type calling procedure. Related to Figure 1.

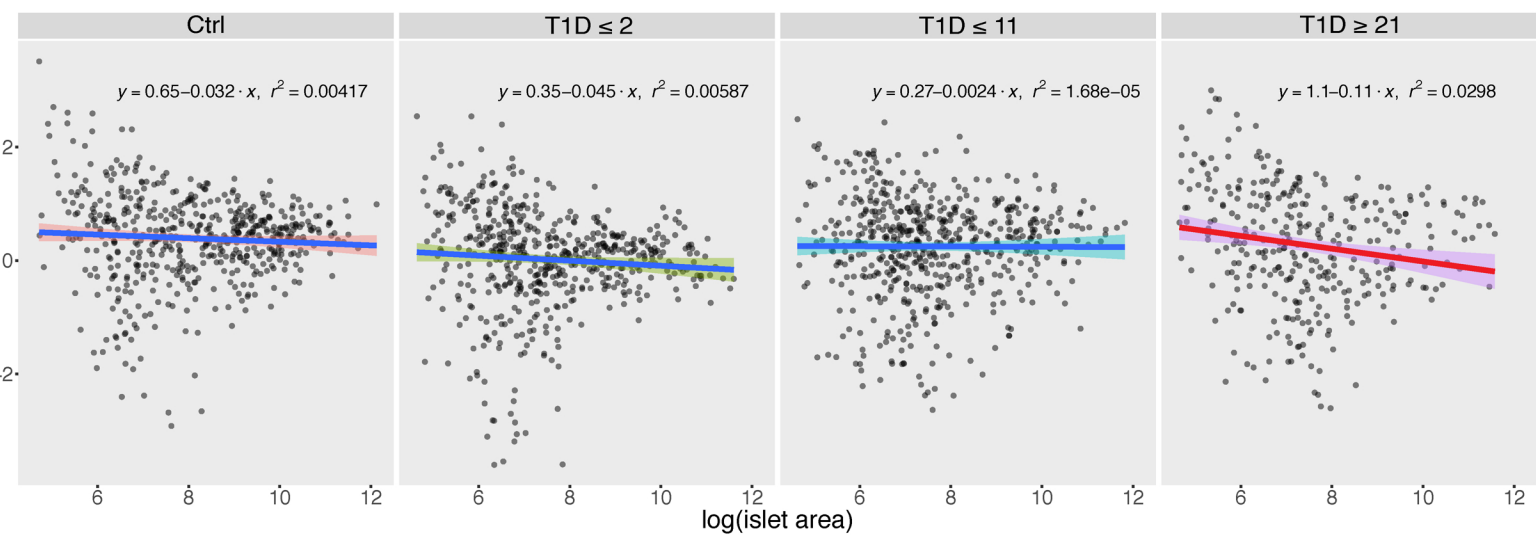
- (A) Pixel compensation between spillover channels. Compensation between CD14 (spillover contributing channel) and NESTIN (spillover influenced channel) is shown as an example. Note the reduction in channel crossover for pixels with high expression of CD14 post compensation.
- (B) Islet mask.
- (C) Top row: an example of cell masks for non-immune cells. Middle and bottom rows illustrate the thresholding procedure. Bottom row, distribution of C-PEP signals from all the cells within the same ROI is modeled by normal mixtures. Modes of different normal distributions are depicted by colored vertical lines. The thick red line indicates the position of the final threshold. Middle row, cells with C-PEP expression below this chosen threshold are labeled as C-PEP negative population and annotated in golden brown color (left); whereas cells with C-PEP expression above the chosen threshold are labeled as C-PEP positive population and annotated in bright yellow color (right). Their coordinates are projected back to the original staining micrograph to ensure the accuracy of thresholding.
- (D) Example of immune cell masks (top row) and the thresholding procedure for immune channels (middle and lower rows).
- (E-F) Manual cell type calling and systematic cell type calling agree well with each other for both the endocrine cell types (E) and immune cell types (F). Regression equations with r^2 are shown in the top left corner of each graph.
- (G-H) Automated cell type calling is insensitive to different cell masks. For both endocrine cells (G) and immune cells (H), the correlation coefficient is more than 0.98 for different sets of masks generated independently by two different researchers.



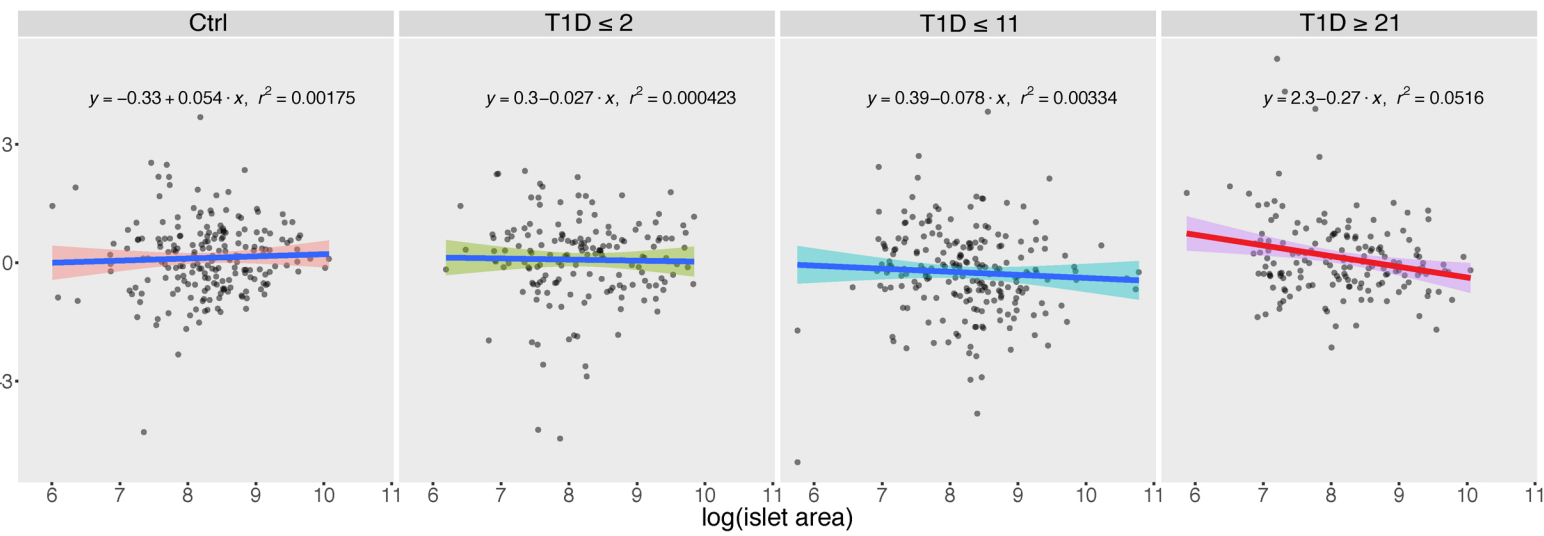
Supplemental Figure 3. Validation of the IMC platform. Related to Figure 1.

- (A) Heatmap demonstrates the expected marker expressions for different cell types. Input data are mean levels of each protein in each cell type. Values associated with each column of the heatmap are centered and standardized separately. Heatmap color indicates Z-score
- (B) Signal comparisons of five hormone channels between IMC and CyTOF. Non-C-PEP hormones are shown in pairwise density plots against C-PEP. Top row corresponds to IMC signals. Bottom row corresponds to CyTOF signals.
- (C-D) Comparison of IMC and single cell suspension CyTOF measurement of endocrine cell populations. The percentage of different endocrine cell types are plotted for HPAP006 (C) and HPAP014 (D).

A

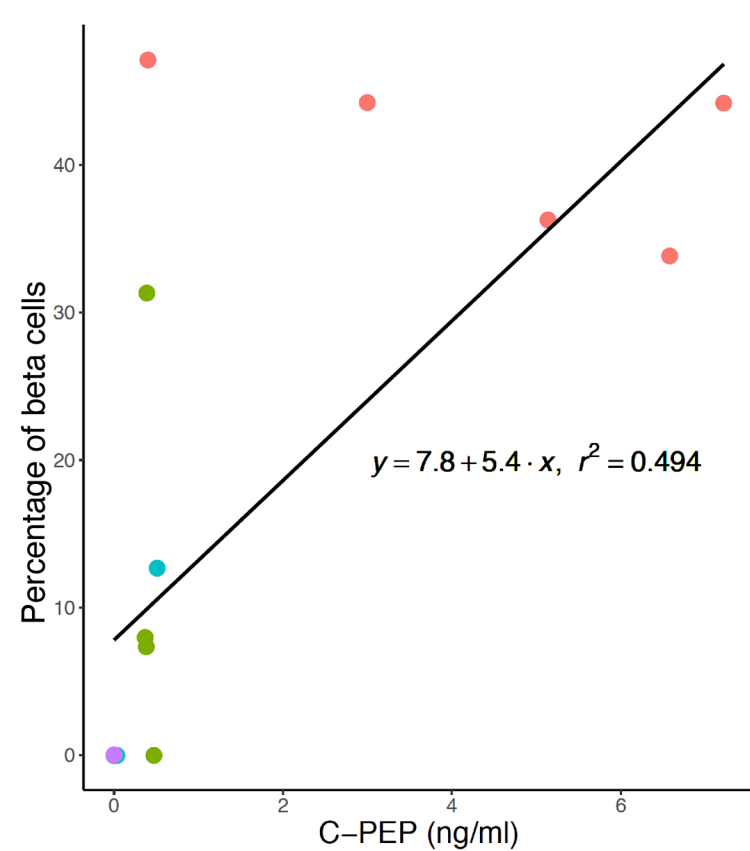


B



Supplementary Figure 4. Modeling of the relationship between islet size and intra-islet vascular density as well as peri-islet collagen area. Red lines indicate statistical significance, measured by linear regression t-test with $p < 0.05$. Related to Figure 2.

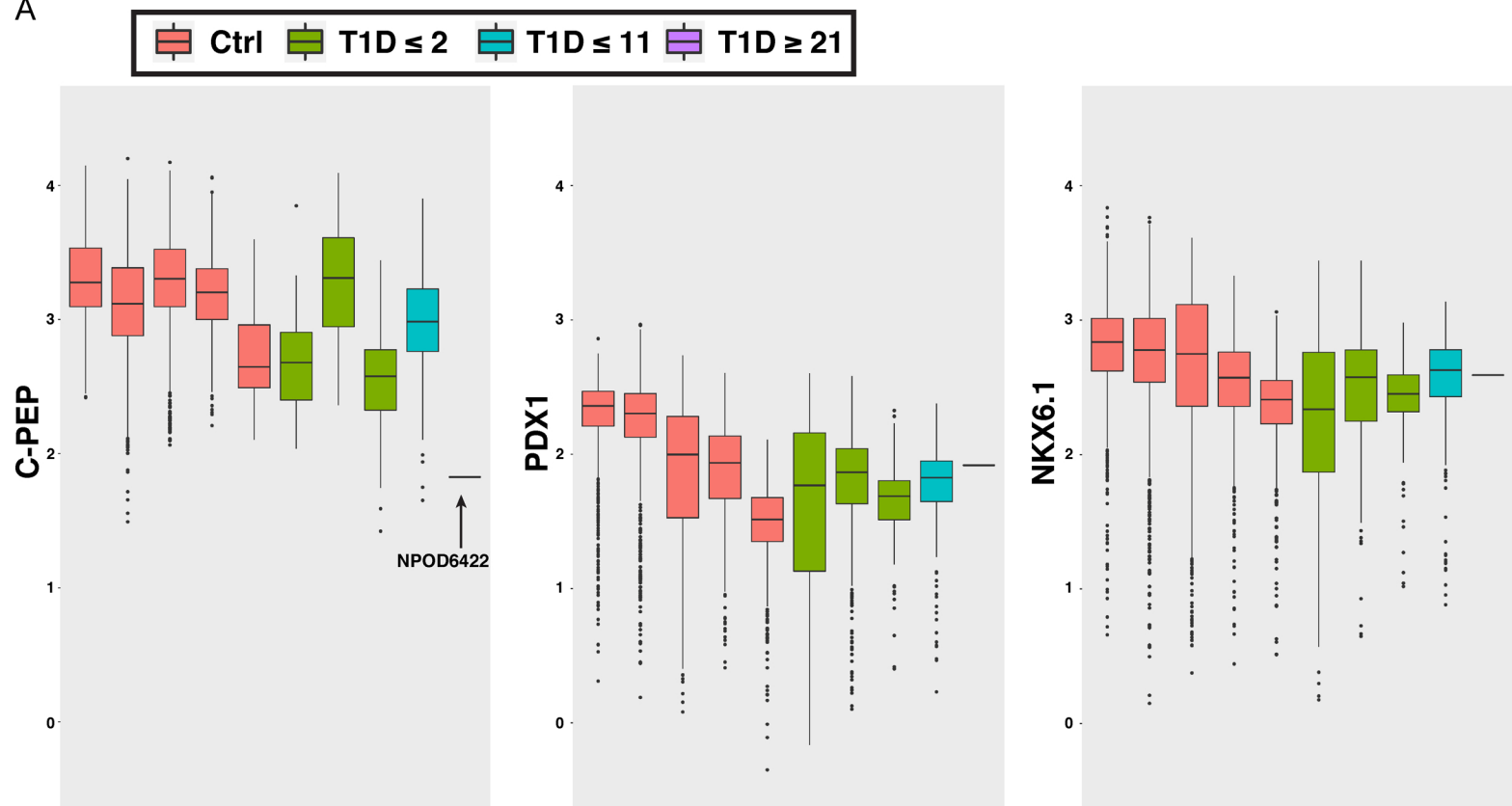
- (A) In the T1D ≥ 21 donor group, increased islet size is associated with reduced vascular density. Each dot represents one islet.
- (B) In the T1D ≥ 21 donor groups, increased islet size is associated with reduced peri-islet collagen area. Each dot represents one islet.



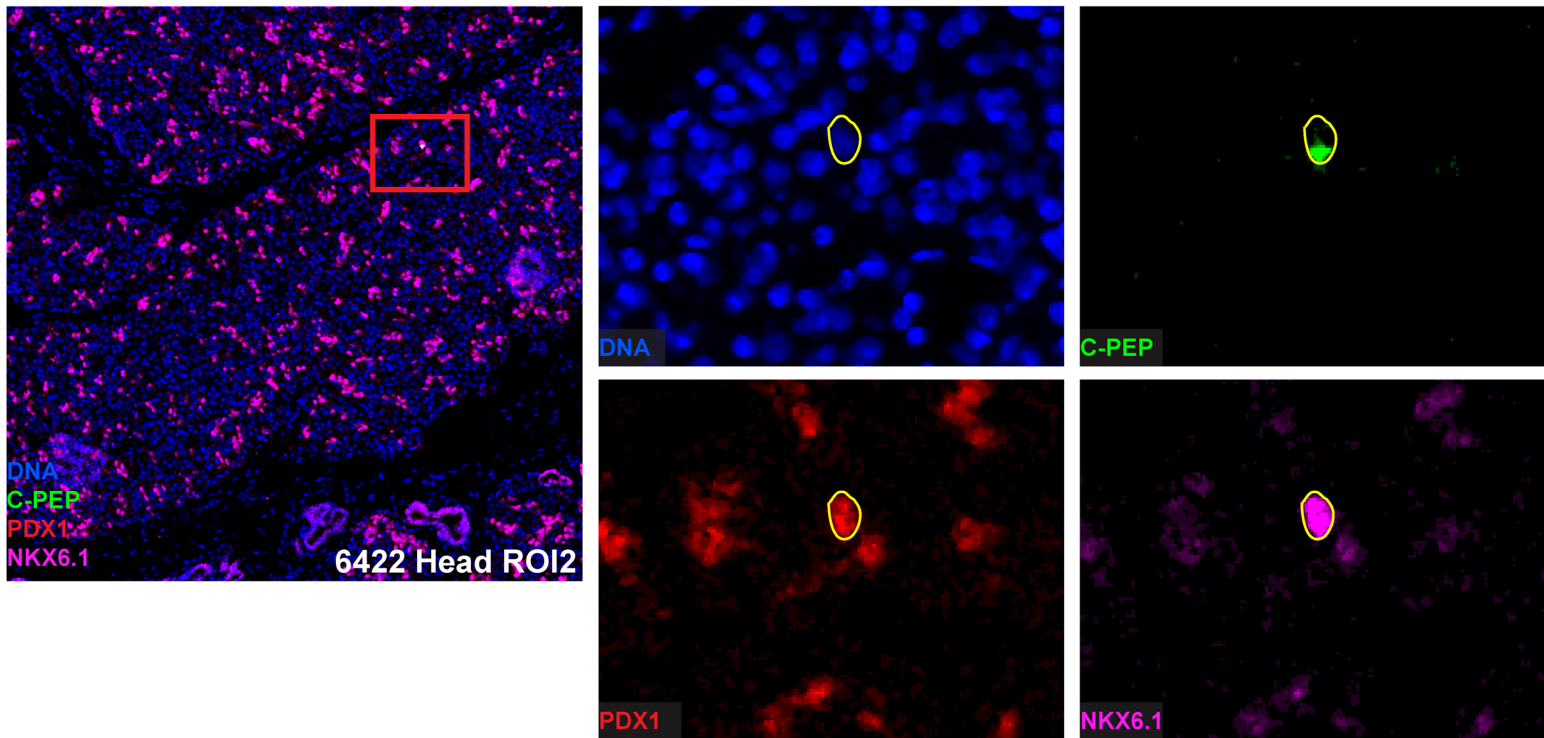
Supplementary Figure 5. Scatter plot demonstrates the correlation between C-PEPTIDE levels in the patients' blood samples and the corresponding beta-cell proportion measured by IMC. Regression function and r^2 is also shown. Linear regression t-test is used to test for statistical significance, with $p < 0.05$. Related to Figure 3.

FIGURE S5

A



B



Supplementary Figure 6. C-PEP, PDX1 and NKX6.1 expressions in the beta cells. Related to Figure 4.

(A) Boxplots display levels of marker proteins in beta cells in individual donor. Each box represents protein expression of beta cells within one donor and is color coded based on donor type. The order of boxplots from left to right is: NPOD6160, NPOD6174, NPOD6389, HPAP005, HPAP006, NPOD6362, NPOD6367, HPAP020, HPAP002, NPOD6422. There is only one beta cell in NPOD6422, and the horizontal line indicates the protein expression level for corresponding marker in this single beta cell.

(B) A single beta cell is found in the pancreas of NPOD6422, a patient with long duration of T1D (T1D \geq 21). This beta cell displays authentic expression of C-PEP (green); PDX1 (red) and NKX6.1 (magenta). DNA-Iridium staining is shown in blue. Panels on the right are zoom-ins from the red boxed area.

Table S1 Antibodies and working concentration. Related to Figure 1.

Mass	Targets	Expression	Concentration in cocktail (ng/µl or dilution#)
141	HLA-ABC	MHCI	6.13
142	CD57	NK and CD8+ T cells	1:100
143	CD31	Endothelial cells	1.57
144	CD14	Monocytes/macrophages	1:200
145	C-PEPTIDE	Beta cells	0.34
146	NESTIN	Endothelial and stromal cells	1:300
147	GLUCAGON	Alpha cells	2.40
148	pan-Keratin	Ductal cells	1:800
149	CD11b	Granulocytes, monocytes/macrophages, dendritic cells	1:100
150	CD44	Ductal and immune cells	1:200
151	PDX-1	Beta, delta, and ductal cells	0.54
152	CD45	Immune cells	1:300
153	CD56	NK cells, subsets of T cells	4.04
154	β-ACTIN	Epithelial cells	1:100
155	FOXP3	Treg	1:25
156	CD4	CD4 T cells	1:100
158	NKX6.1	Beta cells, ductal cells	0.94
159	CD68	Monocytes/macrophages	1:300
160	SOMATOSTATIN	Delta cells	1.26
161	CD20	B cells	1:100
162	CD8	CD8 T cells	1:100
164	CD99	Membrane marker	3.11
165	CA2	Ductal cells	2.50
166	NF-κB	Ductal cells, Cellular signaling	1:300
167	Granzyme B	Cytotoxic T cells, macrophages and NK cells	1:600
168	Ki67	Proliferation	1:300
169	Collagen type I	Stroma	1:200
170	CD3	T cells	1:100
172	pS6	Acinar cells, Cellular signaling	1:100
173	CD45RO	Memory T cell	1:300
174	HLA-DR	MHCII	5.36
175	PANCREATIC POLYPEPTIDE	PP cells	8.41
176	GHRELIN	Epsilon cells	4.04

Concentration in ng/ μ l is given for home-made antibodies; concentration in dilution is given for Fluidigm antibodies.

Table S2 Antibodies that have passed quality assessment. Related to Figure 1.

Targets	Antibodies	Validation		
		Expected tissue localization	Expected co-expression	Consistent staining pattern post metal conjugation
HLA-ABC	BD Biosciences, 565292	Yes		Yes
CD57	Fluidigm, 3142007B	Yes		NA
CD31	LifeSpan BioSciences, LS-C390863-100	Yes	Yes, with NESTIN	Yes
CD14	Fluidigm, 3144025D	Yes	Yes, with CD68	NA
C-PEPTIDE	Thermo, MA1-22710	Yes	Yes, with PDX1	Yes
NESTIN	Fluidigm, 3146015B	Yes	Yes, with CD31	NA
GLUCAGON	Santa Cruz, sc-514592	Yes		Yes
pan-Keratin	Fluidigm, 3148020D	Yes	Yes, with CA2, NF-κB, PDX1 ^{dim} , and NKX6.1 ^{dim}	Yes
CD11b	Fluidigm, 3149028D	Yes		NA
CD44	Fluidigm, 3150018B	Yes		NA
PDX-1	R&D systems, AF2419	Yes	Yes, with C-PEPTIDE, NKX6.1, and SOMATOSTATIN	Yes
CD45	Fluidigm, 3152016D	Yes	Yes, with other immune-cell markers	NA
CD45	Fluidigm, 3152018D	Yes	Yes, with other immune-cell markers	NA
CD56	Proteintech, 14255-1-AP	Yes		Yes
β-ACTIN	Fluidigm, 3154021D	Yes		NA
FOXP3	Fluidigm, 3155016D	Yes		NA

CD4	Fluidigm, 3156033D	Yes	Yes, with CD3	NA
NKX6.1	Sigma, HPA036774	Yes	Yes, with C- PEPTIDE and PDX-1	
CD68	Fluidigm, 3159035D	Yes	Yes, with CD14	NA
SOMATOSTATIN	Santa Cruz, Sc-13099	Yes	Yes, with PDX-1	
CD20	Fluidigm, 3161029D	Yes		NA
CD8	Fluidigm, 3162034D	Yes	Yes, with CD3	NA
CD99	R&D systems, AF3968	Yes		
CA2	Rockland, 200-401-136S	Yes	Yes, with NF-κB , PDX-1 ^{dim} , and NKX6-1 ^{dim}	
NF-κB	Fluidigm, 3166006A	Yes	Yes, with CA2, PDX-1 ^{dim} , and NKX6-1 ^{dim}	NA
Granzyme B	Fluidigm, 3167021D	Yes		NA
Ki67	Fluidigm, 3168022D	Yes		NA
Collagen type I	Fluidigm, 3169023D	Yes		NA
CD3	Fluidigm, 3170019D	Yes	Yes, with CD4 and CD8	NA
pS6	Fluidigm, 3172008A	Yes		NA
CD45RO	Fluidigm, 3173016D	Yes		NA
HLA-DR	Abcam, ab20181	Yes		Yes
PANCREATIC POLYPEPTIDE	Abcam, ab77192	Yes		Yes
GHRELIN	Santa Cruz, sc-10368	Yes		Yes

Antibodies are all tested in FFPE section with antigen retrieval at 95°C in 10mM Tris, 1mM EDTA (pH9.2).

Table S3 Antibodies that have failed quality assessment. Related to Figure 1.

Targets	Antibodies	Validation		
		Expected tissue localization	Expected co-expression	Consistent staining pattern post metal conjugation
CD11b	ThermoFisher Scientific MA1-80091	No		
CD14	Fluidigm 3151009B	No		
CD19	Fluidigm 3169011B	No		
CD3	Fluidigm 3154003B	No		
CD31	Fluidigm 3145004B	No		
CD44	Santa Cruz sc-7297	No		
CD44	Abcam ab157107	No		
CD45	Fluidigm 3089003B	No		
CD49F	Fluidigm 3164006B	No		
CD49F	Santa Cruz sc-374057	No		
CD49F	Novus Biologicals NBP1-85747	No		
CD56	Fluidigm 3149021B	No		
CD56	R&D MAB24081	No		
CD9	ThermoFisher Scientific 14-0098-82	No		
CD9	Santa Cruz sc-13118	Yes		No
CD9	Proteintech 13334	Yes		No
CTLA-4	Fluidigm 3170005B	No		
FOXP3	Fluidigm 3162011A	No		
GCK	Santa Cruz sc-17819	No		
GCK	Abcam ab37796	No		
GCK	Sigma HPA007034	No		
GFAP	Fluidigm 3143022B	No		
GITR	ThermoFisher PA5-46810	Yes		No
GLUT2	Abbiotec 250672	No		
GLUT2	Rockland 600-401-GN3S	No		
GLUT3	Santa Cruz sc-74399	No		
HLA-ABC	Fluidigm 3141010B	No		
HLA-ABC	Bio-Rad MCA485G	No		
HLA-ABC	Proteintech 66013-1-1g	No		
HLA-DR	Fluidigm 3143013B	No		
p21	Santa Cruz sc-6246	Yes		No

PD-1	Abcam ab52587	No		
PD-1	Fluidigm 3174020B	No		
PDGFRA	Fluidigm 3160007A	No		
PDGFRA	Santa Cruz sc-398206	No		
PDGFRA	Novus Biologicals AF-307-NA	No		
Perforin	Fluidigm 3175004B	No		
Perforin	Santa Cruz sc-374346	Yes		No
PDX-1	Santa Cruz sc-14664	No		
ST8SIA1	R&D AF6716	Yes		No

Antibodies are all tested in FFPE section with antigen retrieval at 95°C in 10mM Tris, 1mM EDTA (pH9.2).

Table S4 Donor Information. Related to Figure 1

Group	Case ID	Ethnicity	Age	BMI	Sex	T1D Duration (years)	AAbs	Hb1Ac	C-peptide levels (ng/ml)	Hospital stay duration (days)	Tissue Part (H, B, T*)
Ctrl	NPOD6160	Caucasian	22	23.9	M		Neg	5.2	0.4	2.27	H/B/T
	NPOD6174	Caucasian	21	19.5	M		Neg	NA	3	0.82	H/B/T
	NPOD6389	Caucasian	19	20.9	M		NA	5.1	7.22	2.61	H/B/T
	HPAP005	African American	14	24.1	F		Neg	5.4	5.14	2.96	H/B/T
	HPAP006	Caucasian	46	19.1	M		Neg	5.3	6.58	3.14	H/B/T
	HPAP014	Caucasian	43	30.9	F		Neg	5.7	6.05	3.32	H/B/T
T1D ≤ 2	NPOD6247	Caucasian	24	24.3	M	0.6	IAA	NA	0.47	1.71	H/B/T
	NPOD6362	Caucasian	25	28.5	M	0	GAD65	10	0.38	7.76	H/B/T
	NPOD6367	Caucasian	24	25.7	M	2	Neg	8.8	0.39	4.62	H/T
	HPAP020	Caucasian	14	13.2	M	0	GAD65, IA-2, IAA, ZnT8	NA	0.37	6.79	H/B/T
T1D ≤ 11	NPOD6180	Caucasian	27	25.9	M	11	GAD65, IA-2, IAA, ZnT8	NA	< 0.05	5.53	H/B/T
	NPOD6236	Caucasian	25	20.1	M	11	GAD65, IAA	11.6	< 0.05	3.13	H/B/T
	NPOD6418	Caucasian	25	26.4	M	11	GAD65, IA-2, IAA, ZnT8	7.5	< 0.02	5.25	H/B/T
	HPAP002	Hispanic	26	16.4	M	5	Neg	9.8	0.51	5.96	H/B/T
	HPAP015	Caucasian	29	22	M	7	Neg	NA	0.03	13.48	H/B/T
T1D ≥ 21	NPOD6041	Caucasian	26	28.4	M	23	Neg	NA	< 0.05	3.34	H/B/T
	NPOD6204	Caucasian	28	23.0	M	21	GAD65, IAA	7.2	< 0.05	5.86	H/B/T
	NPOD6422	Caucasian	23	25.1	M	21	NA	7.1	< 0.02	5.48	H/B/T

H, B, T* indicate head, body, tail part of the pancreas correspondingly.

Table S5 Cell type calling rules. Related to Figure 1.

Cell types	Positive Markers	Exclusion Markers
Alpha	GCG	
Beta	C-PEP	
Delta	SST	
PP	PP	GCG
Epsilon	GHRL	
Ductal	CA2 or NF-κB	
Acinar		
Endothelial	CD31 or Nestin	
Immune cells	CD45	CD99high, PDX-1, NKX6.1, CA2
T cells	CD45 and CD3	CD20, CD56 and CD68
B cells	CD45 and CD20	CD3, CD56 and CD68
CD4+ T cells	CD45 and CD3 and CD4	CD8
CD8+ T cells	CD45 and CD3 and CD8	CD4
NK cells	CD45 and CD56	CD3, CD20 and CD68
Macrophages	CD45 and CD68	CD3, CD20 and CD56